

Effect of pressure, temperature, and oxygen fugacity on the metal-silicate partitioning of Te, Se, and S: Implications for earth differentiation

Lesley Rose-Weston^{a,*}, James M. Brenan^a, Yingwei Fei^b, Richard A. Secco^c,
Daniel J. Frost^d

^a *Department of Geology, University of Toronto, Toronto, Canada*

^b *Geophysical Laboratory, Carnegie Institute of Washington, Washington, DC, USA*

^c *Department of Earth Sciences, University of Western Ontario, London, Canada*

^d *Bayerisches Geoinstitut, Universität Bayreuth, Bayreuth, Germany*

Received 9 September 2008; accepted in revised form 8 April 2009; available online 7 May 2009

Abstract

We have measured liquid Fe metal–liquid silicate partitioning (D_i) of tellurium, selenium, and sulfur over a range of pressure, temperature, and oxygen fugacity (1–19 GPa, 2023–2693 K, f_{O_2} –0.4 to –5.5 log units relative to the iron–wüstite buffer) to better assess the role of metallic melts in fractionating these elements during mantle melting and early Earth evolution. We find that metal-silicate partitioning of all three elements decreases with falling FeO activity in the silicate melt, and that the addition of 5–10 wt% S in the metal phase results in a 3-fold enhancement of both D_{Te} and D_{Se} . In general, Te, Se, and S all become more siderophile with increasing pressure, and less siderophile with increasing temperature, in agreement with previous work. In all sulfur-bearing experiments, D_{Te} is greater than D_{Se} or D_S , with the latter two being similar over a range of P and T . Parameterized results are used to estimate metal-silicate partitioning at the base of a magma ocean which deepens as accretion progresses, with the equilibration temperature fixed at the peridotite liquidus. We show that during accretion, Te behaves like a highly siderophile element, with expected core/mantle partitioning of $>10^5$, in contrast to the observed core/mantle ratio of ~ 100 . Less extreme differences are observed for Se and S, which yielded core/mantle partitioning 100– to 10 times higher, respectively, than the observed value. Addition of ~ 0.5 wt% of a meteorite component (H, EH or EL ordinary chondrite) is sufficient to raise mantle abundances to their current level and erase the original interelement fractionation of metal-silicate equilibrium.

© 2009 Elsevier Ltd. All rights reserved.

1. INTRODUCTION

It is generally thought that the Earth accreted over a few tens of millions of years (30–50 Myr; Wetherill, 1994; Halliday, 2004; Kleine et al., 2005) from material of roughly chondritic composition (Ganapathy and Anders, 1974; Anders, 1977; Wolf et al., 1980; Allègre et al., 1995; McDonough and Sun, 1995). During the

accretion process, the conversion of kinetic energy of impactors to heat, and radioactive decay of short-lived isotopes likely caused widespread melting of the growing planet (Sasaki and Nakazawa, 1986; Benz and Cameron, 1990; Tonks and Melosh, 1993). Metallic Fe–Ni liquid would have separated from molten silicate due to density contrast, removing siderophile trace elements to the proto-Earth's center, leaving behind a siderophile-element depleted silicate residue. If core formation involved equilibration between molten metal and silicate on a global scale, this process should have established the siderophile element composition of the residual mantle, in a manner

* Corresponding author.

E-mail address: lesleyannerose@yahoo.ca (L. Rose-Weston).

predictable from high P - T laboratory measurements. For the moderately siderophile elements (MSEs) this seems to be the case, and it is the high pressure convergence of D_{Ni} and D_{Co} which was the basis for the suggestion that equilibrium core formation occurred at the floor of a deep magma ocean (Li and Agee, 1996; Righter et al., 1997; Chabot et al., 2005), although equilibration pressures are probably higher than previously supposed (Kegler et al., 2008). Further support for equilibrium core formation stems from the results of Wood and co-workers (Wade and Wood, 2005; Wood et al., 2006), who matched the mantle abundances of a variety of MSEs (Mo, W, Cr, V, Mn, etc.) with values predicted from high P - T metal-silicate partitioning using a model in which P - T - fO_2 conditions change as the Earth continues to accrete material and grow. With the exception of Pd (Righter et al., 2008), Au (Danielson et al., 2005), and possibly Re (Righter and Drake, 1997), mantle abundances predicted from metal-silicate partitioning of the highly siderophile

elements (HSEs) are significantly lower than observed values (Ohtani et al., 1997; Holzheid et al., 2000; Fortenfant et al., 2003; Cottrell and Walker, 2006; Ertel et al., 2006; Yokoyama et al., 2009). There is some uncertainty, however, in how to apportion the discrete metal grains found in some run product glasses, in terms of a dissolved component, vs. a stable phase present at P and T (Cottrell and Walker, 2006; Ertel et al., 2006). Therefore, the discrepancy between predicted and observed mantle abundances may not be as large as previously supposed. As a consequence of these unresolved issues, the behaviour of the HSE has evoked more complex evolutionary histories of Earth accretion and core formation, requiring the addition of HSE-bearing material to the mantle following initial metal extraction (e.g. Morgan, 1986 and references therein).

The Group VIA elements sulfur, selenium and tellurium, which are volatile, but siderophile and chalcophile, have received little attention in terms of their behaviour during

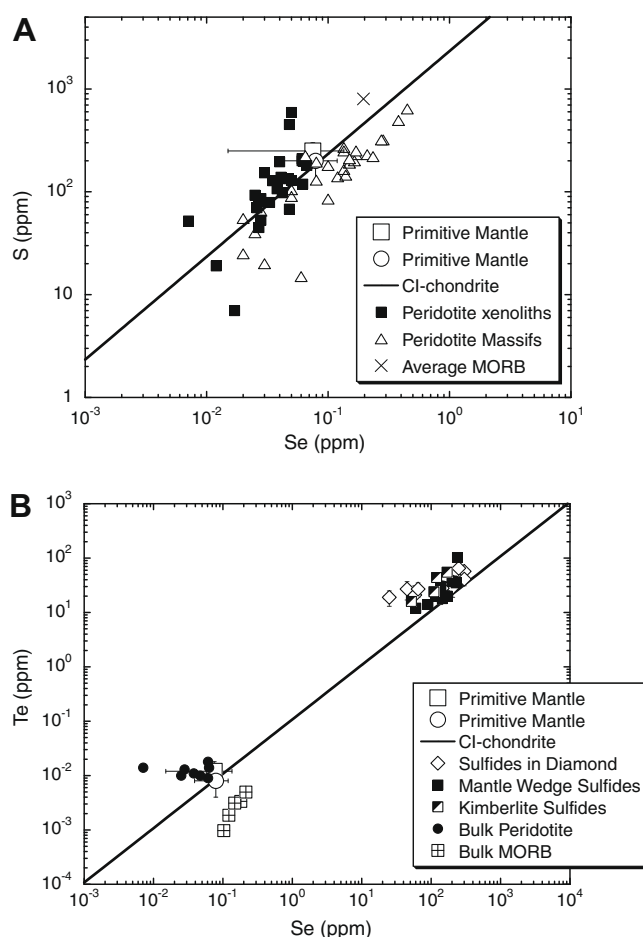


Fig. 1. (A) Abundance of S and Se for peridotite xenoliths (Morgan, 1986; Lorand et al., 2003) and massifs (Garuti et al., 1984), average MORB (Hamlyn et al., 1985 and references therein), and primitive mantle (square: McDonough and Sun, 1995; circle: Palme and O'Neill, 2003). (B) Abundance of Te and Se in upper mantle rocks and primitive magmas (peridotite: Morgan, 1986; MORB: Hertogen et al., 1980), upper mantle sulfides (sulfide inclusions in diamond: Bulanova et al., 1996; sulfides in mantle wedge xenoliths and kimberlites: Hattori et al., 2002), and primitive mantle as in (A). The line through the data in each plot corresponds to the chondritic ratio of Palme and O'Neill (2003). Te is retained in the solid mantle during partial melting compared to Se, as evidenced by the elevated Se/Te in MORB relative to mantle abundances (Hattori et al., 2002).

metal separation in an early Earth. Although they are volatile, Te, Se, and S have nearly the same condensation temperatures (Lodders, 2003), so it is likely they would be available in proportions similar to their chondritic feed-stock during terrestrial accretion. Available estimates of the primitive mantle composition suggest Te, Se, and S are present in chondritic relative abundances (McDonough and Sun, 1995; Palme and O'Neill, 2003; Fig. 1). This result is based on analyses of upper mantle samples, including peridotite xenoliths and massifs (Garuti et al., 1984; Morgan, 1986; Lorand et al., 2003), mid-ocean-ridge basalts (MORB; Hertogen et al., 1980; Hamlyn et al., 1985 and references therein), and mantle sulfides (Bulanova et al., 1996; Hattori et al., 2002). Morgan (1986) showed that both the Se/Re and S/Re ratios in fertile mantle xenoliths are remarkably constant, which combined with a primitive mantle Re content constrained from Re/Os systematics (Morgan, 1985), yield Se and S concentrations of ~ 0.0034 and $0.0032 \times \text{CI}$, respectively. Deviation from a nearly chondritic S/Se in oceanic basalts is likely due to differences in the behaviour of these elements during partial melting (Fig. 1A), although an average value for MORB is not significantly displaced from a chondritic composition (Hamlyn et al., 1985 and references therein). Supra-chondritic Te/Se in residual mantle samples can be ascribed to the relatively less compatible behaviour of Se during partial melting, although the least depleted samples approach the chondritic ratio. The supra-chondritic depletion trend is balanced by MORB samples that are enriched in Se relative to Te. Mantle sulfides that concentrate both Te and Se have chondritic to slightly supra-chondritic Te/Se, also reflecting the effects of partial melting (see below). Abundances of Te, Se, and S in a model primitive mantle (Table 1) show that, like the HSE, Te, Se, and S are depleted from the expected composition of the mantle normalized to CI-chondrite and Mg, and accounting for Earth's volatility trend, thought to

be inherited from the Solar Nebula during accretion (McDonough and Sun, 1995; Lodders, 2003; Palme and O'Neill, 2003). Using the estimated abundance of these elements in the mantle, combined with mass balance involving a volatile-corrected CI-chondrite initial composition, the core–mantle distribution of Te, Se, and S is found to be ~ 100 . If the record of core in-fall is still preserved in the mantle, and this process involved metal–silicate equilibrium, then similar values of $D^{\text{metal-silicate}}$ for Te, Se, and S are required.

Peach et al. (1990) estimated $D_{\text{Se}}^{\text{sulfide-silicate}}$ to be 1770 and $D_{\text{S}}^{\text{sulfide-silicate}}$ to be 393 from coexisting sulfide and silicate melts in mid-ocean ridge basalt. This result is consistent with the preferential retention of Se relative to S in some sulfide-bearing mantle residues (Fig. 1A; Garuti et al., 1984; Hattori et al., 2002), and their slight fractionation in basalts (Hertogen et al., 1980; Hamlyn et al., 1985). Tellurium appears to be more strongly retained than Se (or S) in sulfide-bearing mantle residues, as evidenced by low Te/Se in MORB relative to mantle whole-rocks and sulfides (Fig. 1B; Hertogen et al., 1980; Morgan, 1986; Hattori et al., 2002). This is also consistent with experimental determinations of $D^{\text{sulfide-silicate}}$ for Te and Se, which have shown that Te is more compatible in sulfide compared to Se (Choi and Cho, 1997; Brenan and McDonough, 2006). If sulfide–silicate partitioning behaviour (in which the sulfide portion is FeS) can be used to infer how these elements may behave in metal–silicate systems (where the FeS component is low), the implication of these data is that metal–silicate partition coefficients are not the same for these elements, with values decreasing in the order $\text{Te} > \text{Se} > \text{S}$.

In contrast to estimates from natural samples, similar metal–silicate partitioning for S and Se has been determined separately by Li and Agee (1996) and Li (2000) from experiments done at high P and T (2–20 GPa and 2273 K). The “metallic melt” present in the natural samples and the high P – T experiments are both S-rich, suggesting that the effects of increased pressure and temperature may cause a convergence of partitioning for Se and S. The relatively chondritic Se/S exhibited by upper mantle samples appears to support the notion that abundances record the equilibrium established during core formation. However, the partitioning of Te implied by the super-chondritic Te/Se of natural sulfides (and some peridotites) is not consistent with this conclusion, as the mantle should show a relative depletion of this element.

These empirical estimates of the distribution of Te, Se, and S between metallic and silicate melt are derived from natural systems in which melting occurs at relatively low temperature and pressure, and involving sulfur-rich metallic melt compositions. To improve our understanding of these elements during planetary accretion and differentiation, we have conducted a series of metal–silicate partitioning experiments over a range of elevated pressure and temperature and reducing $f\text{O}_2$ conditions (1–19 GPa, 2023–2693 K, IW-0.4 to IW-5.5). Results are then used to evaluate models of Earth differentiation involving metal–silicate equilibrium, and the possibility of on-going accretion following initial core formation.

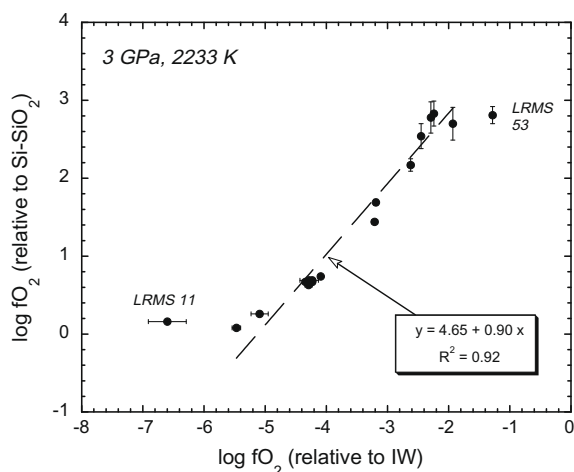


Fig. 2. Comparison of experimental oxygen fugacity calculated relative to the iron–wüstite buffer (IW) and relative to the Si–SiO₂ buffer for samples equilibrated at the same P – T conditions. Samples which plot off the expected linear trend have either unusually low FeO in the silicate phase (LRMS 11), or low Si content in the metal phase (LRMS 53).

Table 1
Core–mantle distribution of Te, Se, and S (ppm).

Reference	Element	CI-chondrite	CI-chondrite (volatile-corrected) ^a	Modeled primitive mantle	Calculated core	Core–mantle distribution (D^*) ^b
McDonough and Sun (1995)	Te	2.33 (0.12)	0.30 (0.02)	0.012 (0.006)	0.898 (0.012)	75 (38)
	Se	21 (1.05)	2.7 (0.14)	0.075 (0.060)	8.15 (0.13)	109 (87)
	S	54,000 (2700)	6350 (324)	250 (50)	19,019 (104)	76 (16)
Palme and O'Neill (2003)	Te	2.27 (0.227)	0.30 (0.03)	0.008 (0.004)	0.906 (0.093)	113 (58)
	Se	21.4 (1.07)	2.78 (0.14)	0.079 (0.040)	8.39 (0.44)	106 (53)
	S	54,100 (2705)	6492 (325)	200 (80)	19,560 (1013)	98 (39)

^a Volatile-depleted values used as bulk starting composition of Earth accretion material.

^b Core–mantle distribution (D^*) is the ratio of calculated core concentration of an element divided by that of the primitive mantle.

2. EXPERIMENTAL PROCEDURE

Powdered metal (Fe + 5 wt% Ni) and silicate (either synthetic basalt or synthetic Allende meteorite; see footnote in [Electronic Annex Table 1](#) for compositions; [Brenan et al., 2003](#); [Jarosewich, 1990](#)) were combined in roughly equal proportions by weight. The silicate starting material was first reduced at FMQ-2 and 1273 K in a gas-mixing furnace, ensuring the dominance of Fe^{2+} over Fe^{3+} . Te and/or Se were added as metal powders between 0.07 and 3 wt% of the metallic portion. Some experiments also contained 9–28 wt% (in the metallic portion) of finely powdered sulfur. Both single- and multi-element experiments were run with variable amounts of Si powder added to alter the oxygen fugacity relative to the iron-wüstite buffering reaction (see below). Starting compositions are listed in [Electronic Annex Table 1](#). Due to the small sample size of most multi-anvil experiments, the metallic portion was pre-fused in evacuated silica tubes and re-ground ensuring the addition of a homogeneous mix. Both piston cylinder and multi-anvil experiments were performed, the details of which are described in the following sections. A summary of the experimental run conditions can be found in [Electronic Annex Table 2](#).

2.1. Piston-cylinder experiments

Experiments at low pressure (1–3 GPa) were performed in end-loaded piston-cylinder apparatus employing 1.27 cm diameter pressure cells at the University of Toronto and the Geophysical Laboratory in Washington, DC (sample LRMS 54). Metallic and silicate powdered samples were packed into pre-sintered MgO crucibles closed with tight-fitting lids. Crucibles were positioned between bottom MgO spacers and top MgO thermocouple insulators (also pre-sintered), and encased in straight-walled graphite heaters. Outer sleeves were composed of concentric cylinders of fused silica and machined talc, or pressed $BaCO_3$, and wrapped in thin Pb foil. A friction correction on the nominal sample pressure was determined for these assemblies using the melting point of diopside ([Boettcher et al., 1982](#)). Temperature was controlled with a type C W-Re thermocouple located directly above the crucible lid. The temperature profile of the assembly was determined by measuring the thickness of a layer of spinel grown between MgO and Al_2O_3 in a separate calibration experiment performed at 1735 °C, 3 GPa, for 30 min, after the method

of [Watson et al. \(2002\)](#). The straight-walled graphite heater produced a thermal gradient within the assemblies, such that the sample temperature (positioned straddling the hot-spot) was 225 K hotter than the value measured at the thermocouple (located 4 mm above). Experimental samples

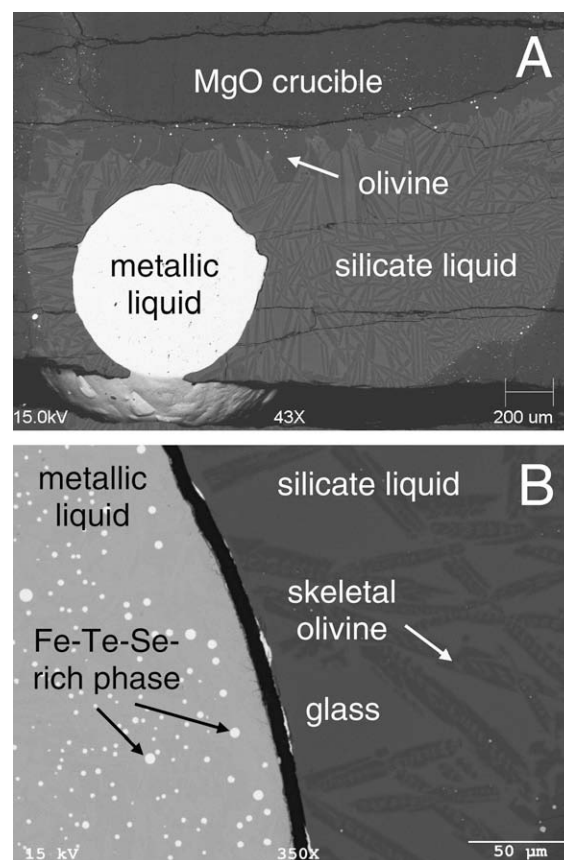


Fig. 3. Backscattered electron images of a sectioned run product (sample LRMS 21 run at 2233 K, 1.9 GPa, and IW-2.9, containing Te and Se). (A) Metal and silicate liquids coalesce at run conditions and are separated by a sharp contact. Stable olivine crystals have grown from the wall of the MgO crucible, trapping a small amount of metal. (B) Close-up of the quench texture in metal and silicate liquids. The metal liquid quenched to an intergrowth of Fe–Ni alloy containing spherical blebs of a Fe–Te–Se-rich phase. Liquid silicate quenched to skeletal olivine crystals and glass. A sharp contact is visible as a dark line between the metallic and silicate liquid portions.

Table 2

Reconstructed silicate melt composition by electron microprobe^a (wt%).

Sample	n ^{ol}	n ^{gl}	Al ₂ O ₃	FeO	MgO	CaO	SiO ₂	Na ₂ O	BaO	S	Total ^c
LRMS 1	6	9	6.66 (0.89) ^b	0.53 (0.07)	35.76 (2.96)	7.57 (0.97)	48.63 (0.89)	0.40 (0.17)	—	—	99.73
LRMS 2	7	14	7.54 (0.76)	5.41 (0.26)	30.44 (2.02)	8.53 (0.77)	46.95 (0.39)	0.47 (0.14)	—	—	99.43
LRMS 3	8	14	11.16 (1.07)	9.53 (0.72)	25.34 (1.69)	12.30 (0.74)	39.69 (0.46)	0.80 (0.05)	—	—	98.95
LRMS 5	7	10	7.70 (1.37)	0.61 (0.05)	33.30 (4.08)	8.73 (1.18)	48.37 (1.23)	0.56 (0.18)	—	—	99.37
LRMS 6	10	18	8.84 (1.07)	0.40 (0.04)	36.77 (2.14)	10.30 (0.89)	41.53 (0.28)	0.76 (0.09)	—	—	99.22
LRMS 7	7	10	6.48 (1.00)	1.66 (0.20)	38.44 (2.22)	7.44 (0.83)	44.61 (0.37)	0.46 (0.12)	—	—	99.17
LRMS 8	4	16	9.09 (1.04)	8.13 (0.18)	30.08 (1.80)	9.71 (0.82)	41.34 (0.24)	0.65 (0.06)	—	—	99.06
LRMS 9	7	11	6.52 (0.62)	0.70 (0.05)	35.89 (1.70)	7.46 (0.70)	48.25 (0.62)	0.41 (0.08)	Below detection	—	99.30
LRMS 10	9	5	8.86 (0.34)	5.41 (0.18)	30.06 (0.82)	9.21 (0.24)	41.76 (0.21)	0.67 (0.03)	3.31 (0.31)	—	99.34
LRMS 11	7	23	4.30 (0.51)	0.02 (0.01)	45.21 (0.40)	7.23 (0.37)	40.27 (0.39)	0.58 (0.03)	0.28 (0.04)	—	100.32
LRMS 12	6	8	7.16 (0.56)	3.66 (0.38)	36.24 (1.15)	7.24 (0.50)	45.22 (0.30)	0.33 (0.12)	Below detection	—	99.99
LRMS 13	4	10	7.70 (0.44)	6.02 (0.38)	32.94 (0.76)	8.33 (0.52)	44.30 (0.28)	0.32 (0.04)	Below detection	—	99.77
LRMS 14	9	8	5.25 (0.59)	0.15 (0.05)	42.79 (1.01)	5.21 (0.41)	45.24 (0.31)	0.24 (0.07)	Below detection	—	99.94
LRMS 15	10	9	6.29 (0.62)	4.13 (0.39)	40.66 (0.95)	7.00 (0.38)	40.33 (0.36)	0.51 (0.05)	—	—	99.11
LRMS 19	9	17	5.03 (0.56)	2.00 (0.13)	46.66 (0.61)	6.06 (0.27)	38.90 (0.44)	0.42 (0.02)	—	—	99.48
LRMS 21	6	9	8.50 (0.90)	2.38 (0.27)	35.15 (2.04)	9.40 (0.97)	42.84 (0.32)	0.61 (0.05)	—	—	99.09
LRMS 33	7	10	8.01 (0.88)	10.44 (0.40)	29.80 (1.77)	8.73 (0.77)	42.28 (0.19)	0.59 (0.06)	—	—	99.98
LRMS 34	4	10	7.64 (0.54)	9.30 (0.39)	33.88 (0.83)	8.29 (0.32)	39.84 (0.23)	0.66 (0.19)	—	0.076 (0.013)	99.77
LRMS 35	3	10	5.11 (0.36)	3.43 (0.13)	45.64 (0.40)	6.01 (0.15)	38.80 (0.28)	0.41 (0.04)	—	—	99.62
LRMS 36	5	10	6.96 (0.43)	4.61 (0.35)	39.96 (0.85)	7.83 (0.41)	39.46 (0.23)	0.46 (0.02)	—	0.084 (0.013)	99.45
LRMS 41	6	10	9.67 (1.24)	6.52 (0.33)	31.76 (2.25)	10.92 (1.09)	39.86 (0.47)	0.76 (0.08)	—	0.069 (0.013)	99.64
LRMS 42	5	11	8.19 (0.61)	7.25 (0.41)	30.89 (1.37)	8.13 (0.53)	43.81 (0.34)	0.55 (0.08)	—	0.067 (0.007)	98.95
LRMS 43	8	11	7.31 (0.58)	8.56 (0.47)	31.46 (1.33)	7.54 (0.48)	43.63 (0.23)	0.51 (0.07)	—	0.071 (0.012)	99.17
LRMS 44	6	7	5.57 (0.52)	1.37 (0.10)	41.64 (1.29)	6.11 (0.52)	43.48 (0.24)	0.41 (0.04)	—	0.138 (0.033)	99.14
LRMS 45	7	9	5.08 (0.64)	0.36 (0.13)	42.76 (1.94)	5.35 (0.74)	44.44 (0.46)	0.34 (0.05)	—	0.774 (0.103)	99.16
LRMS 46	4	9	4.92 (0.55)	0.08 (0.01)	43.51 (1.44)	4.91 (0.57)	43.10 (0.15)	0.29 (0.04)	—	2.726 (0.309)	100.38
LRMS 47	5	11	8.01 (0.99)	8.31 (0.19)	28.91 (2.63)	8.41 (1.02)	45.39 (0.54)	0.49 (0.13)	—	0.054 (0.011)	99.63
LRMS 48	4	11	7.81 (1.04)	0.51 (0.05)	34.32 (2.93)	8.25 (1.03)	47.84 (0.64)	0.56 (0.08)	—	—	99.48
LRMS 50	3	10	5.17 (0.27)	10.80 (0.49)	34.99 (0.70)	5.14 (0.53)	44.28 (0.35)	0.23 (0.08)	Below detection	0.019 (0.009)	100.67
LRMS 53	6	10	3.44 (0.63)	9.47 (1.11)	38.69 (1.06)	6.69 (0.99)	37.73 (0.68)	0.51 (0.19)	2.62 (0.59)	0.110 (0.033)	99.32
LRMS 54	11	11	3.72 (0.60)	4.01 (0.48)	46.13 (1.09)	5.41 (0.58)	39.26 (0.55)	0.34 (0.06)	—	0.120 (0.036)	99.07
UWO 30	5	10	3.58 (0.06)	9.45 (2.09)	36.58 (1.54)	9.83 (0.18)	39.54 (0.35)	0.88 (0.04)	—	—	99.96
GL-388	19		4.88 (2.19)	6.01 (1.17)	46.47 (3.31)	4.88 (2.08)	37.53 (2.10)	0.06 (0.03)	—	0.401 (0.212)	100.47
BGI-J	12		2.82 (1.01)	7.54 (0.88)	44.89 (3.01)	6.41 (2.16)	39.89 (0.91)	0.21 (0.10)	—	0.280 (0.092)	102.13
BGI-E	13		3.00 (0.48)	5.22 (1.11)	40.28 (1.95)	10.06 (1.09)	40.82 (1.12)	0.29 (0.03)	—	0.218 (0.079)	99.87
BGI-L	17		3.47 (0.40)	11.48 (0.79)	41.60 (1.29)	4.89 (0.53)	40.27 (0.54)	0.09 (0.01)	—	0.118 (0.042)	102.00
BGI-K	12		3.13 (0.24)	9.88 (0.55)	40.29 (1.08)	5.47 (0.49)	41.67 (0.33)	0.34 (0.05)	—	0.133 (0.039)	101.00
3B.5	10		3.54 (1.77)	8.12 (0.97)	42.90 (3.55)	5.68 (1.82)	39.29 (1.28)	0.21 (0.07)	—	0.103 (0.099)	101.37 ^d
BGI-A	20		2.70 (0.37)	6.33 (0.39)	43.70 (1.47)	4.79 (0.63)	41.91 (0.31)	—	—	0.423 (0.192)	99.85
BGI-M	19		3.78 (0.36)	10.58 (0.69)	37.68 (1.30)	6.11 (0.57)	43.08 (0.48)	0.17 (0.02)	—	0.061 (0.009)	101.57
3B.6	7		3.81 (0.75)	5.32 (0.44)	43.14 (5.57)	6.77 (1.69)	40.12 (3.17)	0.28 (0.06)	—	0.076 (0.029)	100.90 ^d
BGI-N	22		3.21 (0.23)	10.78 (1.04)	37.86 (1.44)	5.15 (0.39)	44.00 (0.56)	0.12 (0.01)	—	0.056 (0.016)	101.23
3B.7	15		4.45 (0.31)	6.04 (0.41)	41.10 (1.15)	6.89 (0.50)	40.89 (1.10)	0.34 (0.04)	—	0.101 (0.033)	101.55 ^d
3B.8	17		6.33 (0.23)	6.43 (0.26)	36.40 (0.77)	7.90 (0.31)	42.41 (0.69)	0.46 (0.07)	—	0.021 (0.012)	100.98 ^d

^a Final silicate composition for samples having separate glass and olivine analyses reconstructed by determining volume proportions of each phase in the quenched silicate portion, and weighting the phases by considering the density of each phase. Reported error is from chemical analysis only. Samples without separate glass and olivine phases were analyzed using a defocused beam.

^b 1σ standard error about the mean of *n* analyses for each olivine and glass phase, or the combined silicate portion. Error associated with the volume proportions of each phase was not incorporated.

^c Totals include the Te and Se data of Table 3.

^d Totals include trace (<0.05 wt%) amounts of Cr, Mn, Ni, Cu, Se, Sn, Te, W, Au, Pb, and Bi.

experienced near-isothermal conditions, however, as the length of the hotspot was the same as that of the sample. Temperatures at the thermocouple and hotspot positions are listed in [Electronic Annex Table 2](#), along with the temperature offset.

Samples were pressurized to slightly above final run conditions and then heated to the run temperature using a programmable controller ramping at either 50 or 100 K/min. Upon reaching final run temperature and allowing 5 min

for stabilization, the piston was backed-out to the desired run pressure. With the exception of time-series experiments, samples were at final *P–T* conditions for 30 min, and were quenched by switching off the heater power supply.

2.2. Multi-anvil experiments

Higher pressure partitioning experiments (5–19 GPa) were conducted in multi-anvil presses at the University of

Western Ontario (Canada), the Geophysical Laboratory (Washington, DC), and the Bayerisches Geoinstitut (Germany). In detail, the presses included: (1) 500-tonne Walker-style press at the University of Western Ontario (14/8 octahedron size), (2) 1500-tonne press with fixed anvils at the Geophysical Lab (18/11 octahedron size), and (3) 1000-tonne press with fixed anvils at the Bayerisches Geoinstitut (14/8 and 10/5 octahedra sizes). Both Cr-doped (BGI and 3B series experiments) and Cr-free (experiments UWO 30 and GL-388) MgO octahedra were employed. Heaters consisted of Nb foil (experiment UWO 30), graphite (experiment GL-388), and $LaCrO_3$ (BGI and 3B series experiments). All experiments used ZrO_2 insulators. Both sintered MgO inner sample containers and single-crystal MgO crucibles were used (as indicated in [Electronic Annex Table 2](#)).

Multi-anvil experiments were pressurized over ~ 4 h and then heated to run temperature by manually increasing controller output power in small increments (~ 100 K/min). Temperature inside the assembly was monitored with a type D W-Re thermocouple located above the MgO sample lid. In some experiments the thermocouple was compromised, necessitating the use of a temperature-power relationship (derived from multiple successful experiments) to estimate controller temperature. Similar to the piston-cylinder experiments, temperatures at the sample position in multi-anvil experiments are higher than those recorded by the thermocouple. The magnitude of the temperature offset between thermocouple and sample was determined using in-house calibrations at the University of Western Ontario for sample UWO 30. The results of [van Westrenan et al. \(2003\)](#) were applied to estimate the temperature offset of sample GL-388 and the BGI-series experiments contained within crushable MgO capsules. Use of single-crystal MgO crucibles in other BGI-series experiments and the 3B series experiments increased the temperature offset to 420 K between thermocouple and sample position. First reported by [Asahara et al. \(2007\)](#), this temperature offset was evaluated using the melting point of Pt at 10 GPa, taken to be 2323 K from the work of [Kavner and Jeanloz \(1998\)](#). Such an extraordinary temperature offset is thought to be the result of the insulating properties of single-crystal MgO and also the relative hardness of this sample container compared to polycrystalline MgO, which pushed the thermocouple towards the top of the assembly during compression, as seen during inspection of the sectioned run product.

Multi-anvil experiments were held at final pressure and temperature conditions between 1.5 and 30 min. The shorter run duration was thought to be long enough to ensure chemical equilibration between metal and silicate liquids, yet short enough to avoid substantial reaction of the sample with the MgO sample container. Experiments were quenched by terminating the power to the heater.

3. ANALYTICAL METHODS

3.1. Major element analysis by electron microprobe

Quenched experiments were mounted in epoxy, sectioned, and polished using SiC and alumina powder in

preparation for analysis. Silicate melts quenched to discrete phases of skeletal olivine crystals and silicate glass, while metallic liquid quenched to heterogeneous alloy ([Fig. 3A and B](#)). Major element (including sulfur) composition of silicate and metal were determined with a Cameca SX50 electron microprobe (EMPA) at the University of Toronto, and a JEOL JXA-8200 Superprobe at the Bayerisches Geoinstitut. Conditions of analysis include an accelerating voltage of 15 kV and beam current of 25–30 nA. A focused beam was used to analyze silicate glass and dendritic olivine in most samples. This information was used to reconstruct the melt composition using the mass fractions of skeletal olivine crystals and silicate glass determined in back-scattered electron images of sectioned run products. In cases where the quench intergrowth was too fine, a 30–50 micron defocused beam was used to measure the liquid composition. In samples with coarsely-grained quench texture, the silicate melt composition was determined by both techniques (i.e. reconstruction and broad beam analysis), resulting in good agreement. The metallic phase was also analyzed with a defocused beam between 5 and 80 microns (depending on the texture), to include all quench phases. Elements were standardized against Te metal (Te), ZnSe (Se), Fe metal or hematite (Fe), pentlandite (Ni, S), wollastonite (Si, Ca), MgO (Mg), Al_2O_3 (Al), $MnTiO_3$ (Mn), albite (Na), and barite (Ba). On-peak counting of 10 s was applied for major elements and 60 s for less concentrated elements, such as S in the silicate portion. Raw count rates were converted to element concentrations using a ZAF correction program at both analytical facilities. Compositions of the silicate and metal portions of experiments are presented in [Tables 2 and 4](#), respectively.

3.2. Te and Se analysis by laser ablation ICP-MS

The Te and Se contents of the silicate portions of run products are near or below the detection limit of the electron microprobe and abundances were therefore determined by laser ablation ICP-MS at the University of Toronto and the Bayerisches Geoinstitut. The University of Toronto system employs a frequency-quintupled Nd:YAG laser operating at 213 nm, coupled to a VG PQ-Excell quadrupole ICP-MS. The Bayerisches Geoinstitut system consists of an Elan DRC-e quadrupole mass spectrometer attached to a Geolas M 193 nm ArF Excimer Laser system. Both facilities flush the ablation cell with He to enhance sensitivity ([Eggins et al., 1998; Günther and Heinrich, 1999](#)). A synthetic basalt glass standard for Te and Se was synthesized by fusing a mixture of high purity oxides (SiO_2 , Al_2O_3 , MgO, $CaCO_3$, FeO, and PbO) and elemental powders (Te, Sb, Mo, and Se). The resultant olive-green transparent glass was determined to be homogenous to within 4% (Te) and 1.6% (Se), based on multiple LA-ICP-MS analyses. A portion of this material was dissolved and analyzed for Te and Se by the method of standard addition ICP-MS and determined to contain 62 ppm Te and 490 ppm Se.

Run-product analyses used a laser spot size 50–160 μm in diameter, and typically 3–8 spots were ablated in the quenched silicate portion of each experiment. Analysis

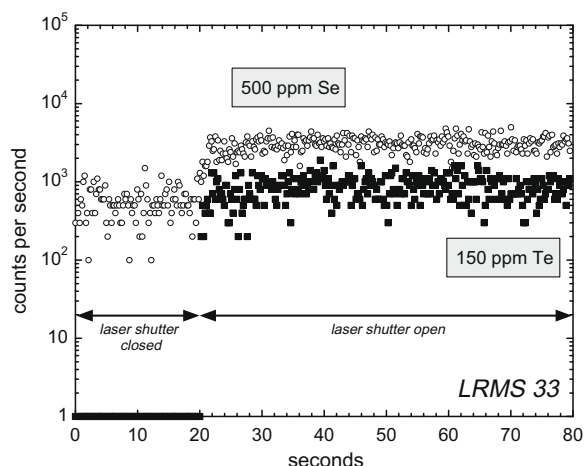


Fig. 4. Time-resolved profile from LA-ICP-MS analysis of quenched silicate liquid from sample LRMS 33 containing Te and Se, run at ~ 3 GPa, 2233 K and IW-1.8. Instrument background is counted for ~ 20 s, followed by laser ablation of the sample for ~ 80 s. For plotting purposes, count rates of zero are plotted as one.

began with 20–30 s of background acquisition followed by 60–70 s of sample ablation. An example of a time-resolved spectrum is shown in Fig. 4. Analyses were acquired in sequence with the first and last three on the synthetic glass standard. Ablation yields in different phases were corrected by reference to the known concentration of Ca in the reconstructed silicate phase as determined by EMPA. Although the quenched silicate is a mixture of olivine and glass, we have determined that ablation yields for these materials are essentially identical. Data reduction was done at the University of Toronto using the GLITTER software package (version 5.3; Macquarie Research, Ltd.), and at BGI using an ‘in-house’ application employing data reduction techniques of Longerich et al. (1996). Element concentrations were determined using multiple isotopes of Te and Se (^{125}Te , ^{126}Te , ^{128}Te , ^{130}Te , ^{76}Se , ^{77}Se , ^{78}Se , ^{82}Se) as a check on potential interferences, and excellent agreement was obtained for each. Te and Se concentrations reported in Table 3 are from ^{125}Te and ^{77}Se , corresponding to the most abundant (^{125}Te) or highest peak/background (^{77}Se) of the isotopes measured.

3.3. Calculating oxygen fugacity ($f\text{O}_2$)

Oxygen fugacity ($f\text{O}_2$) was varied in experiments by adding different amounts of Si to the starting mixture. Silicon partitions into the metal phase under reducing conditions (below IW-1; Kilburn and Wood, 1997). By changing the Si/O in the silicate portion, the activity of FeO in the silicate liquid ($a_{\text{FeO}}^{\text{silicate}}$) and Fe in the metal ($a_{\text{Fe}}^{\text{metal}}$) are also altered. The $f\text{O}_2$ of an experiment can be calculated with reference to the heterogeneous equilibrium between iron and an oxide phase,



which has an equilibrium constant (k_{eq}) of the form,

Table 3

Concentration of Te and Se in silicate portion by LA-ICP-MS (ppm).

Sample	<i>n</i>	^{125}Te	^{77}Se
LRMS 1	3	1239 (12)	—
LRMS 2	4	172 (5)	—
LRMS 3	3	512 (18)	—
LRMS 5	3	450 (12)	—
LRMS 6	3	—	5879 (247)
LRMS 7	3	111 (4)	—
LRMS 8	3	94 (2)	—
LRMS 9	3	199 (4)	—
LRMS 10	4	150 (12)	—
LRMS 11	6	20,126 (1438)	—
LRMS 12	3	—	718 (10)
LRMS 13	3	—	719 (6)
LRMS 14	4	—	10,480 (772)
LRMS 15	3	263 (4)	1010 (12)
LRMS 19	3	861 (53)	2634 (49)
LRMS 20	—	n/a	n/a
LRMS 21	3	389 (7)	1323 (14)
LRMS 33	3	153 (22)	502 (17)
LRMS 34	3	51 (7)	227 (7)
LRMS 35	3	573 (25)	1151 (61)
LRMS 36	3	112 (2)	438 (3)
LRMS 41	3	25 (4)	166 (5)
LRMS 42	3	16 (3)	141 (3)
LRMS 43	3	37 (6)	173 (7)
LRMS 44	6	59 (9)	396 (14)
LRMS 45	3	29 (2)	322 (5)
LRMS 46	3	3881 (44)	4449 (53)
LRMS 47	3	7 (1)	37 (1)
LRMS 48	4	1292 (28)	—
LRMS 50	6	23 (6)	109 (8)
LRMS 53	3	52 (2)	226 (1)
LRMS 54	3	160 (58)	535 (83)
UWO 30	3	178 (97)	110 (12)
GL-388	3	863 (264)	1267 (119)
BGI-J	6	61 (44)	56 (20)
BGI-E	3	8 (4)	23 (5)
BGI-L	4	7 (2)	Below detection
BGI-K	2	Below detection	Below detection
3B.5	5	18 (2)	172 (15)
BGI-A	3	14 (4)	43 (6)
BGI-M	2	11 (1)	Below detection
3B.6	3	25 (2)	198 (3)
BGI-N	3	Below detection	Below detection
3B.7	6	26 (13)	142 (27)
3B.8	6	3.21 (0.85)	33 (4)

$$k_{\text{eq}} = \left(\frac{a_{\text{FeO}}}{a_{\text{Fe}}} \right) (f\text{O}_2)^{-\frac{1}{2}} \quad (2)$$

and, by reference to the iron-wüstite (IW) buffer yields the expression,

$$\log f\text{O}_2(\Delta\text{IW}) = 2 * \log \left(\frac{a_{\text{FeO}}^{\text{silicate}}}{a_{\text{Fe}}^{\text{metal}}} \right) \quad (3)$$

The activity of the Fe species in the metal and silicate phases are defined as:

$$a_{\text{Fe}}^{\text{metal}} = \gamma_{\text{Fe}}^{\text{metal}} * X_{\text{Fe}}^{\text{metal}} \quad (4)$$

$$a_{\text{FeO}}^{\text{silicate}} = \gamma_{\text{FeO}}^{\text{silicate}} * X_{\text{FeO}}^{\text{silicate}} \quad (5)$$

For experiments containing mostly Fe in the metallic portion, we assume that the activity of Fe in the metal liquid is equal to its mole fraction. Some experiments contained an appreciable amount of S in the metallic portion, however, causing the activity-composition relations to become more complex. In this case, the activity coefficient of Fe (γ_{Fe}^{metal}) was determined using the model of Kress

(2007) for Fe–Ni–S–O liquids. Values of γ_{Fe}^{metal} calculated in this fashion are reported in Table 5. Because the MgO content of our experiments is between 25 and 47 wt%, a single $\gamma_{FeO}^{silicate}$ is not appropriate. We have employed the formulation of O'Neill and Eggins (2002) to calculate $\gamma_{FeO}^{silicate}$ for each silicate melt composition, with results listed in Table 5. As demonstrated by Toplis (2005), the effect of pressure

Table 4
Metallic liquid composition (wt%).

Sample	n	Fe	Ni	Si	Te	Se	S	Total
LRMS 1	9	86.81 (0.54) ^a	5.92 (0.08)	5.20 (0.03)	2.54 (0.38)	—	—	100.47
LRMS 2	25	92.65 (0.52)	4.75 (0.12)	0.06 (0.02)	2.51 (0.41)	—	—	99.97
LRMS 3	8	90.71 (0.64)	5.71 (0.18)	—	3.68 (0.70)	—	—	100.11
LRMS 5	10	90.29 (0.20)	3.68 (0.03)	4.78 (0.02)	0.81 (0.11)	—	—	99.55
LRMS 6	10	90.75 (0.19)	5.11 (0.06)	3.85 (0.03)	—	0.90 (0.05)	—	100.61
LRMS 7	9	94.24 (0.22)	5.11 (0.05)	0.70 (0.02)	0.92 (0.06)	—	—	100.98
LRMS 8	10	94.63 (0.21)	4.90 (0.05)	0.04 (0.02)	1.03 (0.09)	—	—	100.60
LRMS 9	9	92.45 (0.44)	3.83 (0.06)	3.99 (0.03)	0.60 (0.20)	—	—	100.88
LRMS 10	9	94.42 (0.44)	5.11 (0.03)	0.03 (0.02)	1.50 (0.30)	—	—	101.06
LRMS 11	10	81.41 (0.30)	4.33 (0.06)	13.19 (0.13)	0.28 (0.08)	—	—	99.21
LRMS 12	10	92.85 (0.31)	5.59 (0.04)	0.13 (0.03)	—	2.33 (0.25)	—	100.91
LRMS 13	10	94.46 (0.18)	4.02 (0.04)	0.03 (0.01)	—	2.37 (0.14)	—	100.89
LRMS 14	10	84.35 (0.21)	3.41 (0.06)	11.63 (0.10)	—	0.589 (0.07)	—	99.98
LRMS 15	11	90.00 (0.71)	5.97 (0.06)	0.06 (0.04)	2.28 (0.31)	2.02 (0.48)	—	100.32
LRMS 19	10	92.61 (0.59)	4.75 (0.13)	0.02 (0.01)	1.31 (0.21)	1.43 (0.27)	—	100.12
LRMS 20 (solid)	10	95.30 (0.53)	4.66 (0.13)	0.13 (0.02)	0.11 (0.03)	0.17 (0.12)	—	100.37
LRMS 20 (liquid)	8	72.08 (5.31)	4.35 (1.51)	0.07 (0.02)	8.63 (5.84)	14.90 (4.50)	—	100.04
LRMS 21	11	91.12 (0.64)	5.11 (0.07)	0.14 (0.10)	1.42 (0.30)	1.32 (0.28)	—	99.11
LRMS 33	9	92.24 (0.59)	5.08 (0.07)	—	1.59 (0.18)	1.52 (0.31)	—	100.43
LRMS 34	10	82.20 (1.08)	4.01 (0.09)	—	1.65 (0.25)	2.05 (0.28)	9.70 (0.46)	99.61
LRMS 35	10	93.34 (0.70)	5.52 (0.10)	—	0.98 (0.35)	0.68 (0.47)	—	100.52
LRMS 36	11	93.39 (0.93)	4.70 (0.11)	0.03 (0.01)	0.19 (0.04)	0.36 (0.06)	1.55 (0.30)	100.21
LRMS 41	11	86.18 (0.38)	3.27 (0.04)	—	0.61 (0.08)	1.48 (0.26)	9.08 (0.33)	100.62
LRMS 42	10	85.65 (0.73)	4.22 (0.09)	—	0.51 (0.05)	1.23 (0.21)	9.44 (0.70)	101.05
LRMS 43	11	84.22 (0.75)	3.07 (0.10)	—	1.64 (0.19)	1.98 (0.27)	9.88 (0.62)	100.80
LRMS 44	12	85.37 (0.33)	5.12 (0.11)	0.40 (0.04)	0.94 (0.15)	1.35 (0.29)	7.33 (0.37)	100.52
LRMS 45	11	82.16 (0.27)	4.94 (0.08)	4.24 (0.09)	0.17 (0.03)	0.30 (0.16)	9.15 (0.44)	100.95
LRMS 46	11	74.89 (0.34)	7.01 (0.10)	17.22 (0.17)	0.189 (0.067)	0.05 (0.02)	0.41 (0.11)	99.84
LRMS 47	21	83.40 (0.77)	4.91 (0.18)	0.03 (0.02)	0.644 (0.120)	0.50 (0.24)	11.57 (0.66)	101.05
LRMS 48	15	89.20 (0.92)	4.74 (0.07)	4.68 (0.11)	2.17 (1.09)	—	—	100.79
LRMS 50	11	84.94 (0.80)	4.98 (0.12)	0.03 (0.01)	1.66 (0.18)	2.09 (0.15)	6.49 (0.41)	100.19
LRMS 53	10	76.35 (0.97)	6.11 (0.30)	0.03 (0.01)	1.81 (0.41)	2.28 (0.16)	12.86 (0.78)	99.44
LRMS 54	11	78.76 (1.51)	5.80 (0.34)	0.03 (0.01)	0.66 (0.12)	2.32 (0.22)	12.13 (1.22)	99.63
UWO 30	14	83.30 (1.46)	7.83 (0.46)	—	6.63 (1.23)	2.35 (0.31)	—	100.12
GL-388	14	71.39 (0.92)	6.39 (0.15)	0.02 (0.01)	3.02 (0.12)	3.12 (0.14)	15.64 (0.73)	99.57
BGI-J	17	78.15 (0.95)	5.83 (0.25)	—	0.22 (0.03)	0.28 (0.05)	13.32 (0.81)	97.80
BGI-E	23	74.04 (0.90)	6.27 (0.29)	—	0.22 (0.06)	0.36 (0.03)	14.28 (0.50)	97.34 ^b
BGI-L	17	80.60 (1.36)	5.35 (0.24)	—	0.20 (0.04)	0.25 (0.04)	11.92 (0.90)	98.32
BGI-K	15	80.60 (0.83)	5.40 (0.11)	—	0.19 (0.04)	0.25 (0.03)	11.41 (0.67)	97.84
3B.5	20	69.18 (0.74)	7.25 (0.36)	—	0.89 (0.11)	1.39 (0.09)	11.33 (0.75)	95.06 ^c
BGI-A	9	51.77 (0.72)	13.29 (0.80)	—	0.65 (0.11)	0.57 (0.03)	32.62 (0.29)	98.89
BGI-M	15	81.46 (1.09)	5.61 (0.19)	—	0.17 (0.03)	0.24 (0.04)	10.96 (1.09)	98.45
3B.6	20	75.56 (0.97)	5.80 (0.16)	—	0.90 (0.12)	1.36 (0.08)	11.02 (0.59)	99.10 ^d
BGI-N	15	81.46 (0.95)	5.57 (0.15)	—	0.18 (0.03)	0.25 (0.03)	10.87 (0.81)	98.33
3B.7	15	74.37 (1.61)	6.02 (0.16)	—	1.11 (0.15)	1.51 (0.14)	11.16 (1.14)	99.21 ^e
3B.8	21	74.81 (0.75)	6.64 (0.13)	—	0.88 (0.03)	1.26 (0.08)	10.23 (0.42)	98.51 ^f

^a 1 σ standard error about the mean of n analyses.

^b Total includes 1.46 wt% W, 0.42 wt% Pt, and 0.20 wt% O.

^c Total includes 0.71 wt% Sn, 0.49 wt% W, 0.29 wt% Pb, 0.83 wt% Bi, 1.33 wt% Au, 0.33 wt% Cu, 1.04 wt% O.

^d Total includes 0.77 wt% Sn, 0.62 wt% W, 0.36 wt% Pb, 0.43 wt% Bi, 1.13 wt% Au, 0.29 wt% Cu, 0.87 wt% O.

^e Total includes 0.84 wt% Sn, 0.77 wt% W, 0.36 wt% Pb, 0.59 wt% Bi, 1.35 wt% Au, 0.28 wt% Cu, 0.85 wt% O.

^f Total includes 0.74 wt% Sn, 0.66 wt% W, 0.46 wt% Pb, 0.56 wt% Bi, 1.25 wt% Au, 0.25 wt% Cu, 0.77 wt% O.

Table 5
Activity coefficients of Fe and FeO and calculated oxygen fugacity (fO_2).

Sample	γ_{Fe}^{metal}	$\gamma_{FeO}^{silicate}$	$\log fO_2$ (ΔIW)	$\log fO_2$ ($\Delta Si-SiO_2$)
LRMS 1	1.00	1.54	−4.29 (0.06)	0.63 (0.01)
LRMS 2	1.00	1.37	−2.45 (0.02)	2.54 (0.16)
LRMS 3	1.00	1.61	−1.77 (0.03)	—
LRMS 5	1.00	1.49	−4.23 (0.04)	0.67 (0.01)
LRMS 6	1.00	2.31	−4.23 (0.04)	0.69 (0.01)
LRMS 7	1.00	1.93	−3.21 (0.05)	1.44 (0.01)
LRMS 8	1.00	1.65	−1.93 (0.01)	2.70 (0.21)
LRMS 9	1.00	1.56	−4.09 (0.03)	0.74 (0.01)
LRMS 10	1.00	1.61	−2.29 (0.01)	2.78 (0.20)
LRMS 11 ^a	1.00	3.06	−4.99 (0.31)	0.16 (0.01)
LRMS 12	1.00	1.70	−2.62 (0.05)	2.17 (0.08)
LRMS 13	1.00	1.60	−2.24 (0.03)	2.83 (0.16)
LRMS 14	1.00	2.04	−5.09 (0.14)	0.26 (0.01)
LRMS 15	1.00	2.39	−2.22 (0.04)	2.47 (0.28)
LRMS 19	1.00	3.23	−2.64 (0.03)	2.86 (0.10)
LRMS 21	1.00	1.95	−2.87 (0.05)	2.12 (0.31)
LRMS 33	1.00	1.50	−1.79 (0.02)	—
LRMS 34	0.99	1.87	−1.55 (0.02)	—
LRMS 35	1.00	3.04	−2.22 (0.02)	—
LRMS 36	1.00	2.48	−2.10 (0.03)	2.84 (0.23)
LRMS 41	1.00	1.96	−1.85 (0.02)	—
LRMS 42	1.00	1.48	−1.98 (0.02)	—
LRMS 43	1.00	1.48	−1.84 (0.02)	—
LRMS 44	1.00	2.13	−3.19 (0.03)	1.69 (0.04)
LRMS 45	1.00	2.10	−4.28 (0.15)	0.69 (0.01)
LRMS 46	1.00	2.13	−5.47 (0.07)	0.08 (0.01)
LRMS 47	0.98	1.33	−1.90 (0.01)	2.88 (0.29)
LRMS 48	1.00	1.54	−4.34 (0.05)	0.67 (0.01)
LRMS 50	1.00	1.47	−1.70 (0.02)	2.90 (0.14)
LRMS 53	0.97	2.30	−1.28 (0.05)	2.81 (0.11)
LRMS 54	0.98	2.96	−1.88 (0.05)	2.83 (0.15)
UWO 30	1.00	2.26	−1.50 (0.10)	—
GL-388	0.95	3.00	−1.41 (0.08)	2.97 (0.12)
BGI-J	0.97	2.71	−1.41 (0.05)	—
BGI-E	0.96	2.62	−1.69 (0.09)	—
BGI-L	0.98	2.12	−1.28 (0.03)	—
BGI-K	0.98	1.99	−1.46 (0.02)	—
3B.5	0.99	2.49	−1.35 (0.02)	—
BGI-A	0.38	2.26	−0.42 (0.03)	—
BGI-M	0.98	1.75	−1.51 (0.03)	—
3B.6	0.99	2.64	−1.74 (0.01)	—
BGI-N	0.99	1.64	−1.56 (0.04)	—
3B.7	0.99	2.30	−1.74 (0.01)	—
3B.8	0.99	1.81	−1.89 (0.01)	—

^a Oxygen fugacity (fO_2) calculated relative to the IW and Si–SiO₂ buffer reactions, as discussed in the text. Sample LRMS 11 fO_2 relative to IW originally −6.60(0.31), adjusted based on fO_2 relative to Si–SiO₂ buffer using equation in Fig. 2.

on the value of $\gamma_{FeO}^{silicate}$ is negligible. Values of fO_2 relative to the IW buffer are reported in Table 5. As a check on oxygen fugacity values calculated relative to the IW buffer, fO_2 was also calculated relative to the Si–SiO₂ buffer for those samples with measurable Si in the metallic phase. Assuming that the activities of both SiO₂ in the silicate portion and Si in the metal portion are equal to their mole fractions, fO_2 relative to the Si–SiO₂ buffer was calculated according to the following expression, and also reported in Table 5.

$$\log fO_2(\Delta Si-SiO_2) = \log \left(\frac{a_{SiO_2}^{silicate}}{a_{Si}^{metal}} \right) \quad (6)$$

When plotted against one another, the experimental fO_2 values relative to both the Si–SiO₂ and IW buffers for samples run at the same P – T conditions are expected to produce a linear trend, indicating a constant offset (Fig. 2). With the exception of samples LRMS 11 and 53 (which are not included in the weighted linear fit), this is indeed the case. It is likely that the fO_2 calculated relative to the IW buffer is incorrect for sample LRMS 11, as the FeO content in the silicate portion of this sample is very low. Conversely, sample LRMS 53 has a very small amount of Si in the metal phase, therefore the estimate of fO_2 relative to the Si–SiO₂ buffer is likely inaccurate. Consequently, we have shifted the fO_2 value of sample LRMS 11 in Table 5 from IW-6.60 to IW-4.99, using the linear expression in Fig. 2.

4. RESULTS

4.1. General appearance

At experimental conditions, the intricately mixed powders of silicate and metal melted and segregated into two discrete liquid phases, separated by a sharp interface (Fig. 3B). Upon quench, the metal exsolved a Te- and/or Se-rich phase (depending on starting composition) present as evenly-disseminated μ m-sized spherical blebs. Silicate liquid quenched to tabular and skeletal olivine crystals, and glass. Equant olivine crystals, interpreted to have been stable at run conditions, nucleated and grew on the surrounding MgO crucible walls. Some metal is seen to have been trapped by the growing olivine crystals. The crucible absorbed FeO from the experimental sample, forming ferropericlase. No Te, Se, or S was detected in either the stable olivine crystals or ferropericlase portion of the MgO crucible. The initial silicate composition became more MgO-rich during the experiment, due to the use of MgO crucibles. Some experiments run in the piston-cylinder with BaCO₃ pressure media contain up to a few percent BaO in the silicate liquid (Table 2), however no Ba was detected in the metal portion by electron microprobe. Liquid metal–liquid silicate partition coefficients ($D_i^{metal-silicate}$) are summarized in Table 6.

4.2. Chemical equilibrium and Henry's law

Experiments were performed at ~ 3 GPa and 2233 K for different duration (7, 15, 30 and 50 min) to establish the onset of chemical equilibrium. Equilibrium, as implied by constant partitioning, is reached after 7 min for S and 15 min for Te and Se (Fig. 5). Equilibrium is also indicated by the homogeneity of both the metallic sphere and the silicate portions, as determined by multiple analyses. No evidence of zoning in either portion was detected by transect analysis. An experimental duration of 30 min was applied to experiments below 3 GPa, whereas most multi-anvil experiments were maintained at run temperature for between 1.5 and 8 min. This shorter run duration was necessary in order

Table 6

Liquid metal–liquid silicate partition coefficients (D).

Sample	$\log D_{\text{Te}}$	$\log D_{\text{Se}}$	$\log D_{\text{S}}$
LRMS 1	1.31 (0.07) ^a	—	—
LRMS 2	2.16 (0.07)	—	—
LRMS 3	1.86 (0.08)	—	—
LRMS 5	1.25 (0.06)	—	—
LRMS 6	—	0.19 (0.03)	—
LRMS 7	1.92 (0.03)	—	—
LRMS 8	2.04 (0.04)	—	—
LRMS 9	1.48 (0.15)	—	—
LRMS 10	2.00 (0.09)	—	—
LRMS 11	−0.86 (0.13)	—	—
LRMS 12	—	1.51 (0.05)	—
LRMS 13	—	1.52 (0.03)	—
LRMS 14	—	−0.25 (0.06)	—
LRMS 15	1.94 (0.06)	1.30 (0.10)	—
LRMS 19	1.18 (0.07)	0.73 (0.08)	—
LRMS 20 ^b	−1.88 (0.24)	−1.94 (0.25)	—
LRMS 21	1.56 (0.09)	1.00 (0.09)	—
LRMS 33	2.02 (0.08)	1.48 (0.09)	—
LRMS 34	2.51 (0.09)	1.96 (0.06)	2.11 (0.04)
LRMS 35	1.23 (0.16)	0.77 (0.30)	—
LRMS 36	1.22 (0.09)	0.91 (0.07)	1.26 (0.11)
LRMS 41	2.38 (0.09)	1.95 (0.08)	2.12 (0.08)
LRMS 42	2.50 (0.10)	1.94 (0.07)	2.15 (0.06)
LRMS 43	2.65 (0.08)	2.06 (0.06)	2.14 (0.08)
LRMS 44	2.20 (0.09)	1.53 (0.10)	1.73 (0.11)
LRMS 45	1.77 (0.07)	0.97 (0.23)	1.07 (0.06)
LRMS 46	−0.31 (0.15)	−0.98 (0.17)	−0.83 (0.13)
LRMS 47	2.95 (0.09)	2.13 (0.21)	2.33 (0.09)
LRMS 48	1.23 (0.22)	—	—
LRMS 50	2.85 (0.12)	2.28 (0.04)	2.53 (0.20)
LRMS 53	2.55 (0.10)	2.01 (0.03)	2.07 (0.13)
LRMS 54	1.61 (0.18)	1.64 (0.08)	2.00 (0.14)
UWO 30	2.57 (0.25)	2.33 (0.08)	—
GL-388	1.55 (0.13)	1.39 (0.05)	1.59 (0.23)
BGI-J	1.56 (0.32)	1.69 (0.17)	1.68 (0.15)
BGI-E	2.46 (0.26)	2.19 (0.11)	1.82 (0.16)
BGI-L	2.45 (0.14)	—	2.01 (0.16)
BGI-K	—	—	1.93 (0.13)
3B.5	2.70 (0.08)	1.91 (0.05)	2.04 (0.42)
BGI-A	2.66 (0.14)	2.12 (0.06)	1.89 (0.20)
BGI-M	2.20 (0.09)	—	2.26 (0.08)
3B.6	2.66 (0.07)	1.94 (0.03)	2.16 (0.17)
BGI-N	—	—	2.29 (0.13)
3B.7	2.60 (0.22)	2.00 (0.09)	2.04 (0.15)
3B.8	3.46 (0.12)	2.61 (0.06)	2.70 (0.25)

^a Errors of $\log D$ -values (y) calculated using $s_y = \frac{s_x}{x \ln 10}$.^b Partition coefficients for Te and Se of LRMS 20 are values calculated between solid and liquid metal.

to prevent excessive reaction between the silicate portion of the sample and the MgO container. Longer experimental duration promoted olivine growth at the expense of the silicate liquid portion, hindering analysis by LA-ICP-MS, which requires between 50 and 100 micron spot sizes to obtain Te and Se values above detection. Owing to the much higher temperatures of multi-anvil experiments, it is likely that equilibrium was rapidly attained.

Experiments were doped with Te, Se, and S in concentrations much higher than natural systems, so Henrian behaviour was evaluated to determine if experimental re-

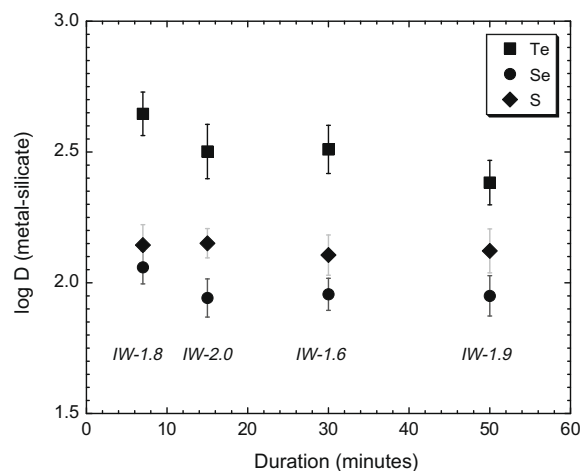


Fig. 5. Metal-silicate partitioning as a function of run duration performed at ~ 3 GPa, 2233 K, and between IW-1.6 and IW-2.0. Constant partitioning is achieved after ~ 15 min for Te and Se, and ~ 7 min for S.

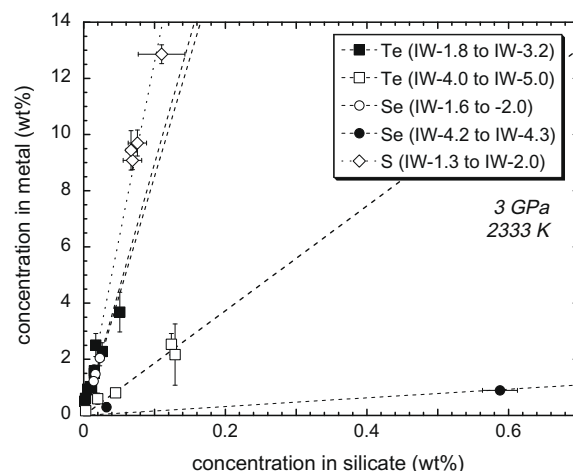


Fig. 6. Te, Se, and S content of the metal liquid as a function of abundance in the silicate liquid. Results are from experiments conducted at ~ 3 GPa, 2233 K and similar fO_2 (see legend). Curves through the data correspond to linear fits forced through the origin.

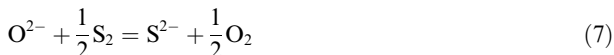
sults can be applied to more dilute systems. Fig. 6 shows Te, Se, and S concentrations in the metal phase as a function of concentrations in the silicate phase (wt%). The resulting linear trends demonstrate that all three elements follow Henry's Law in the concentration range studied.

4.3. Effect of P , T , and fO_2 on metal-silicate partitioning

4.3.1. Theoretical considerations

Although the following theoretical discussion applies specifically to S, owing to their similar chemical properties, we expect that both Se and Te will behave in an analogous fashion. Results of experiments have shown that at oxygen fugacities more reducing than the FMQ buffer, S dissolves

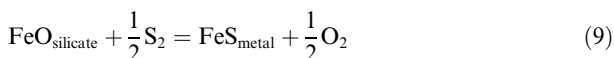
into molten silicate by displacing oxygen anions (Metrich et al., 2005); this has also been confirmed for Se by spectroscopy (e.g., Lipovskii et al., 2008). The following reaction describes the solution behaviour of S under reducing conditions in silicate melt (Fincham and Richardson, 1954; Mavrogenes and O'Neill, 1999):



which can be described by the pseudo-equilibrium constant, known as the sulfide capacity (C_S),

$$C_S = \left\{ \text{S/ppm}^{\text{silicate}} (f\text{O}_2/f\text{S}_2)^{1/2} \right\} \quad (8)$$

The equilibrium between FeS-bearing metallic melt, and coexisting silicate melt can be described by the relation:



for which,

$$-\Delta G^\circ(9) = \ln a_{\text{FeS}}^{\text{metal}} - \ln a_{\text{FeO}}^{\text{silicate}} + \ln(f\text{O}_2/f\text{S}_2)^{1/2} \quad (10)$$

Rearranging Eq. (8) for the term $(f\text{O}_2/f\text{S}_2)^{1/2}$ and substituting into Eq. (10) yields the relation,

$$-\Delta G^\circ(9) = \ln a_{\text{FeS}}^{\text{metal}} - \ln a_{\text{FeO}}^{\text{silicate}} + \ln C_S - \ln \text{S/ppm}^{\text{silicate}} \quad (11)$$

The activity of FeS in the metallic phase can be recast as a S concentration, by noting that $a_{\text{FeS}}^{\text{metal}} = (\gamma_{\text{FeS}}^{\text{metal}})(X_{\text{FeS}}^{\text{metal}})$, and therefore, $a_{\text{FeS}}^{\text{metal}} = B * \text{S/ppm}^{\text{metal}}$, in which B is a constant which includes the activity coefficient and mole to wt% conversion factor. Eq. (11) can therefore be recast in terms of a metallic melt-silicate melt partition coefficient:

$$\ln \left(\frac{\text{S/ppm}^{\text{metal}}}{\text{S/ppm}^{\text{silicate}}} \right) = \ln a_{\text{FeO}}^{\text{silicate}} - \ln C_S - \Delta G^\circ(9) - \ln B \quad (12)$$

Eq. (12) indicates that S partitioning is independent of both $f\text{O}_2$ and $f\text{S}_2$, but will vary with melt composition, through both the a_{FeO} term and C_S (Mavrogenes and O'Neill, 1999; Haughton et al., 1974). The quantities C_S and $\Delta G^\circ(9)$ can be described by pressure- and temperature-dependent entropy, enthalpy and volume terms, which yield the form expected for the variation in metal-silicate partitioning with pressure and temperature (Eq. (13); see Mavrogenes and O'Neill, 1999 for a full derivation). The terms C , D , and E are constants for a given silicate melt composition, and can be determined by experiment.

$$\ln \left(\frac{\text{S/ppm}^{\text{metal}}}{\text{S/ppm}^{\text{silicate}}} \right) = \frac{C}{T} + D + \frac{EP}{T} \quad (13)$$

4.3.2. Dependence of $D_{\text{Te,Se}}^{\text{metal-silicate}}$ on S content and $f\text{O}_2$

Some experiments were 'single-element', as only Te or Se was added to the starting mixture. Others contained both elements, and another set contained Te, Se, and S. At relatively constant $f\text{O}_2$, metal-silicate partitioning of both Te and Se is not affected by the addition of the other, however both D_{Te} and D_{Se} increase by ~ 3 times with the addition of 5–10 wt% S in the metal phase (Fig. 7). Metal-silicate partitioning of Te, Se, and S was investigated as a function

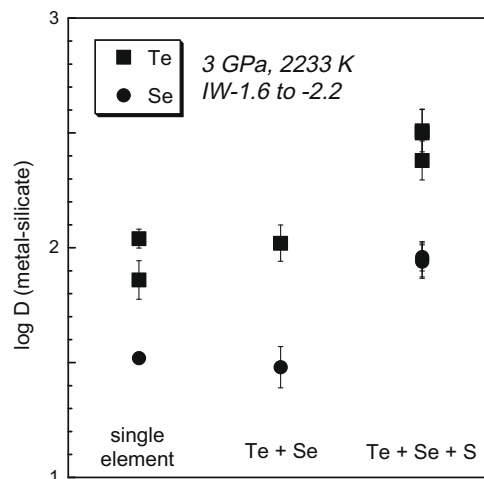


Fig. 7. The effect of added sulfur on D_{Te} and D_{Se} for experiments performed at similar $f\text{O}_2$. Experiments containing only Te or Se, and those containing both Te and Se display constant partitioning. Both D_{Te} and D_{Se} increase when ~ 5 –10 wt% S is incorporated into the metallic phase.

of $f\text{O}_2$ at fixed pressure (3 GPa) and temperature (2233 K), and results are portrayed in Fig. 8. We found that D values were relatively constant at conditions more oxidizing than IW-3, but all three elements become more lithophile with decreasing $f\text{O}_2$. This finding is similar to that determined for S by Kilburn and Wood (1997). Although sulfur-free experiments (shown in Fig. 8A) done at the lowest $f\text{O}_2$ yielded $D_{\text{Te}} < D_{\text{Se}}$, all other experiments produced consistent partitioning across the entire $f\text{O}_2$ range studied, with $D_{\text{Te}} > D_{\text{S}} > D_{\text{Se}}$. Because the experiment redox is linked to the Fe–FeO equilibrium, with decreased $f\text{O}_2$ more Fe is partitioned into the metallic melt phase, so mass balance dictates that the FeO content of the silicate melt, and hence $a_{\text{FeO}}^{\text{silicate}}$, decrease. Using values of $\gamma_{\text{FeO}}^{\text{silicate}}$ calculated from the formulation of O'Neill and Eggins (2002), we find that the values of $a_{\text{FeO}}^{\text{silicate}}$ decrease by ~ 100 -fold across the investigated $f\text{O}_2$ interval. For the same experiments, values of C_S , calculated using the melt composition parameters of Haughton et al. (1974), vary by ~ 2 -fold. With reference to Eq. (12), the observed decrease in D_S , and likely D_{Se} and D_{Te} as well, is consistent with these melt composition effects. Using the calculated values of $a_{\text{FeO}}^{\text{silicate}}$ and C_S , we have modeled the variation in D_S using Eq. (12). Because of uncertainties in the value of $\Delta G^\circ(9) - \ln B$, we have simply scaled the variation in D_S relative to the value obtained in experiment LRMS 34, which was done at the highest $f\text{O}_2$ investigated. The model therefore assumes that all the variation in D_S is due to changes in silicate melt composition, and that $\gamma_{\text{FeS}}^{\text{metal}}$ in the metallic liquid is constant. Results of the calculation, along with the measured values of D_S , are portrayed in Fig. 8C. With the exception of the lowest $f\text{O}_2$ experiment, the model captures the variation in D_S remarkably well. For the experiment done at the lowest $f\text{O}_2$ (LMRS 46), melt composition effects do not completely describe the reduction in D_S , as the calculated value is ~ 10 times higher than measured. It is notable that the metallic

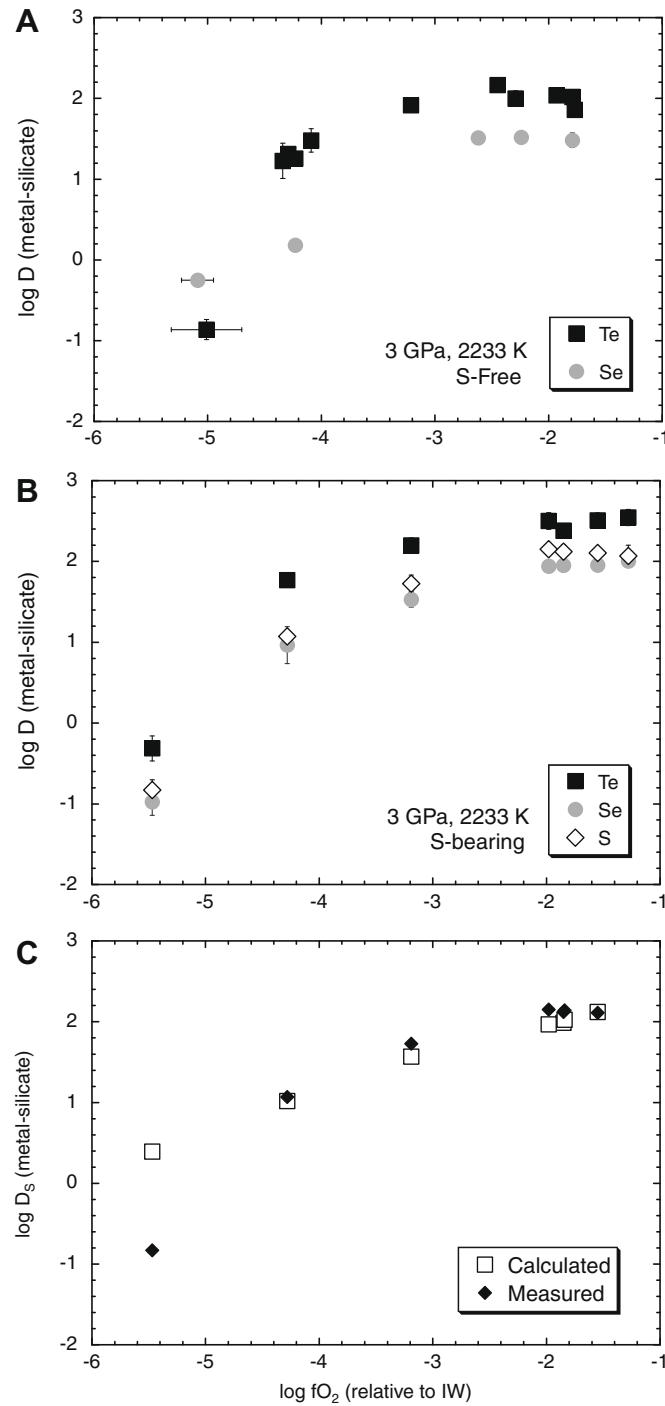


Fig. 8. Effect of variable oxygen fugacity (fO_2) on metal-silicate partitioning of Te, Se, and S for (A) S-free and (B) S-bearing experiments. As in Fig. 7, the addition of S increases D_{Te} and D_{Se} . Increasing fO_2 causes the partition coefficients of all three elements to increase, with D rising sharply under reducing conditions, and less so between IW-3 and IW-1 where partitioning is relatively constant. C) Comparison between calculated (open symbols) and measured (closed symbols) values of D_S for the experiments portrayed in Fig. 8b. In this case, the variation in D_S with fO_2 is modeled to be the result of changes in the activity of FeO and C_S in the silicate melt (see text for discussion).

melt produced in this experiment contains a significant amount of Si (~ 17 wt%) compared to the others, which have 4 wt% or less. Given the high amount of Si, it seems plausible that γ_{FeS} may be different in that composition, so that changes in both silicate and metallic melt compositions have conspired to reduce D_S .

4.3.3. Dependence of $D_{Te,Se,S}^{metal-silicate}$ on temperature and pressure

Experiments were conducted over a range of pressure (1–19 GPa) and temperature (2023–2673 K) within the fO_2 range over which melt composition changes are minimal. Some compositional variation is unavoidable, however, which likely accounts for some of the scatter in the

data. Values of the coefficients C , D , and E in Eq. (13) were determined for each element by multivariate regression. We restricted the regressed dataset to those experiments performed at 2.8 GPa and above (for which linear partitioning is observed), and for compositions covering a restricted compositional range, e.g., activity of FeO in the silicate phase ($a_{\text{FeO}}^{\text{silicate}}$) equal to 0.1 ± 0.02 (corresponding to most runs done at $f\text{O}_2$ of IW-2 or higher). The limited dataset includes samples LRMS 41, 42, 43, 47, 50, BGI-A, BGI-E, 3B.6, 3B.7, and 3B.8. The temperature was estimated for three of these 10 samples due to thermocouple failure, however as these estimates are based on robust temperature–power curves from multiple successful experiments, we have confidence in these values (see Section 2.2 for more details). The resulting equations to describe metal-silicate partitioning are:

$$\log D_{\text{Te}} = -4.94 + \frac{15,069}{T(\text{K})} + 422.98 \frac{P(\text{GPa})}{T(\text{K})} \quad (14)$$

$$\log D_{\text{Se}} = -4.15 + \frac{12,545}{T(\text{K})} + 313.94 \frac{P(\text{GPa})}{T(\text{K})} \quad (15)$$

$$\log D_{\text{S}} = -4.37 + \frac{13,686}{T(\text{K})} + 217.49 \frac{P(\text{GPa})}{T(\text{K})} \quad (16)$$

The average percent difference between measured and calculated values for the restricted dataset is 6% for Te and Se, and 11% for S. Fig. 9A–C show the pressure dependence of $D_{\text{Te,Se,S}}^{\text{metal-silicate}}$ measured from the present study, along with additional data for Se and S compiled from the literature (S: Li and Agee, 1996; Se and S: Li, 2000; S: Ohtani et al., 1997). Samples plotted in Fig. 9 were produced at variable temperatures (see legends) making it difficult to compare individual experimental results. Instead of correcting these data to a common temperature, we have instead plotted isotherms calculated using Eqs. (14)–(16). All three elements become more siderophile with increased pressure, whereas higher temperatures offset this effect.

5. DISCUSSION

5.1. Te–Se–S fractionation in terrestrial magmas and upper mantle residues

Given mantle sulfur abundances in the range of 150–330 ppm (Lorand, 1990), combined with the relatively low degrees of melting inferred for oceanic basalts, it is likely that such magmas are saturated in a sulfide melt in their source (e.g., Mavrogenes and O'Neill, 1999). Results of our sulfur-bearing experiments show that metal-silicate D_{Te} is larger than D_{Se} , predicting that silicate melts derived from sulfide melt-bearing sources should have lower Te/Se than their residue. Although the metallic melts produced in our experiments are sulfur-poor relative to the FeS stoichiometry of natural sulfide liquids, this trend is indeed seen by comparing the Te/Se of upper mantle sulfides or their host peridotites and MORBs (Fig. 1B; Hertogen et al., 1980; Morgan, 1986). The S/Se of average MORB is slightly elevated compared to chondrite and most upper mantle peridotites (Fig. 1A; Garuti et al., 1984; Hamlyn et al., 1985; Morgan, 1986; Lorand et al., 2003), although

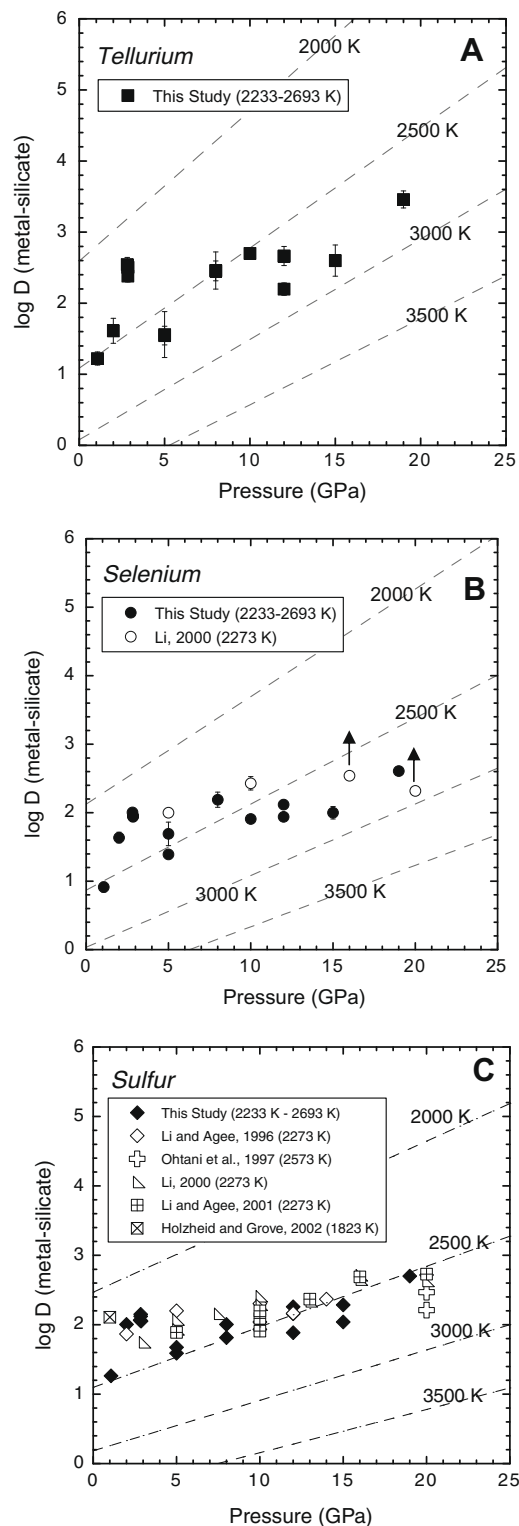


Fig. 9. Metal-silicate partitioning of (A) Te, (B) Se, and (C) S as a function of pressure. Experiments all contain S, and were run over an $f\text{O}_2$ range between IW-0.4 and IW-2.2. Published results for experiments performed under similar temperature conditions are shown for comparison, as are isotherms calculated using Eqs. (14)–(16). Arrows in (B) indicate minimum partitioning values. All three elements are shown to become more siderophile with increasing pressure.

the latter data are somewhat scattered. This suggests that Se is preferentially retained in the sulfide-bearing source during melting compared to S. As mentioned previously, Peach et al. (1990) estimated $D_{\text{Se}}^{\text{sulfide-silicate}}$ to be 1770 and $D_{\text{S}}^{\text{sulfide-silicate}}$ to be 393 from coexisting melts in mid-ocean ridge basalt, which is consistent with the observed S/Se fractionation in MORB (Fig. 1A). Results of the present study show that these two elements partition similarly at high P - T conditions, with a small increase in D_{Se} relative to D_{S} in the experiment involving the most S-rich metallic liquid (32 wt% sulfur; experiment BGI-A). Given that the MORB sulfides measured by Peach et al. (1990) contain ~48 wt% sulfur, we suggest that the difference in D_{S} and D_{Se} seen in MORB is probably due to the high sulfur content of the metallic melt phase.

5.2. Accretion and core formation

The experimental conditions employed in our study allow us to estimate the geochemical consequences of equilibrium metal-silicate separation at P - T conditions that approach those estimated for an early magma ocean. In this context, Wood et al. (2006) and Wade and Wood (2005) present a model of core formation in which metal-silicate equilibrium occurs at the base of a magma ocean which deepens as accretion progresses, and the equilibration temperature is fixed by the peridotite liquidus. With the additional condition that $f\text{O}_2$ increases from IW-4 to IW-2 over the course of core formation, this model provides a close match to the mantle abundances of moderately siderophile elements. We have used the parameterized values of $D^{\text{metal-silicate}}$ measured in this study to determine the behaviour of Te, Se and S in a similar scenario. Like Wade and Wood (2005), our calculations assume that the depth of metal-silicate equilibration in the mantle occurs at half the depth to the core-mantle boundary, and that each aliquot of incoming metal equilibrates with the entire silicate mass before complete chemical isolation in the core. The initial depth of the mantle at 5% accretion is ~1100 km, and the P - T conditions follow the peridotite liquidus (as per Fig. 7 of Wade and Wood, 2005). Therefore at 5% accretion the half depth is ~550 km, the pressure is 18 GPa and temperature 2473 K. With each incremental addition of material the depth increases as well as the P - T conditions. At 100% accretion the half depth of the mantle is ~1500 km, the pressure is 49 GPa and temperature 3389 K. Although we expect that metal-silicate partitioning of Te, Se and S will be intrinsically independent of $f\text{O}_2$, because the redox state of the system is governed by the Fe-FeO equilibrium, changes in $f\text{O}_2$ will certainly change a_{FeO} in the silicate phase, which we have shown to have some effect on partitioning. For the range of $f\text{O}_2$ required by the magma ocean model, we have documented ~5-fold increase of D_{Te} , and a 10-fold increase in D_{S} and D_{Se} with increasing $f\text{O}_2$, or more accurately, increasing a_{FeO} in the silicate phase. Fig. 10 portrays the results of our model calculations for the case of constant $f\text{O}_2$ during accretion (IW-2), and, similar to Wade and Wood (2005), assuming that $f\text{O}_2$ starts at IW-4, increasing to IW-3 at 20% accretion, and IW-2 at 50% accretion. The change in partitioning with $f\text{O}_2$ is modeled

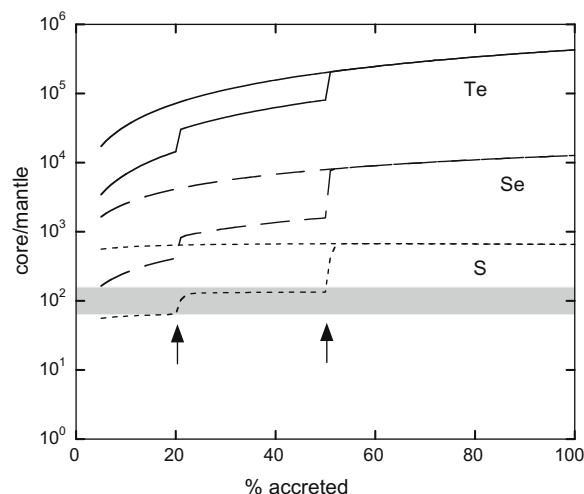


Fig. 10. Calculated core-mantle partitioning as a function of the percentage of Earth accreted assuming that metal-silicate partitioning occurs at the peridotite liquidus at the base of a deepening magma ocean. Continuous curves show element behaviour assuming a constant $f\text{O}_2$ near IW-2, implying a constant a_{FeO} in the silicate phase. Curves showing discontinuities correspond to a model in which the $f\text{O}_2$ is initially at IW-4, implying a low a_{FeO} in the silicate phase, then increases to IW-3 after 20% accretion to a final value of IW-2 after 50% accretion (denoted by arrows). The shaded bar corresponds to the observed core-mantle partitioning of these elements.

crudely by assuming that, relative to the parameterization done for experiments near IW-2, partition coefficients at IW-4 are $5\times$ (Te) and $10\times$ (S, Se) lower at all P - T conditions, rising to $2.5\times$ (Te) and $5\times$ (S, Se) lower at IW-3. In either scenario, it seems clear that there are significant deviations between the partitioning expected from our experiments, and the observed core/mantle ratio of these elements at 100% accretion. Most notable is that our calculations indicate that Te behaves like a highly siderophile element, with expected core/mantle partitioning of $>10^5$, in contrast to the observed core/mantle ratio of ~100. The observed core/mantle partitioning for Se and S is essentially the same as for Te, which contrasts with predicted depletions that are 10- (S) to 100-fold (Se) higher.

As far as our experimental data and calculations allow us to predict, metal-silicate equilibrium during core formation will result in a significant loss of Te relative to Se and S, leading to a sub-chondritic ratio in the silicate mantle, which is not observed. This behaviour is similar to the HSE, whose chondritic abundances in the mantle are inconsistent with the generally large and different metal-silicate partitioning for each of those elements. As discussed by Morgan (1986), the late-stage bombardment of the Earth-Moon system after core separation – so-called heterogeneous accretion model, or “late veneer” – provides a mechanism by which chondritic proportions of HSE can be re-established after removal by the metal phase. Our results suggest that a similar process is responsible for effectively erasing the interelement fractionation and absolute depletion of Te, Se and S resulting from core formation. The quantity of exogenous component required can be

determined by combining our estimates of mantle abundances following core formation with concentrations of Te, Se and S found in candidate meteoritic materials. As discussed by Brandon et al. (2006) and Meisel et al. (2001), the osmium isotopic composition of mantle-derived materials is similar to H-group ordinary and some enstatite chondrites (EH, EL), implying a silicate Earth evolution with similar time-integrated Pt/Os and Re/Os. Selecting these materials as likely components of the late veneer, we have calculated the effect of their addition on the Te, Se and S abundances in the silicate Earth following core formation. We used mean concentrations of Te, Se and S from H, EH and EL-type chondrites reported by Wasson and Kallemeyn (1988), and calculated compositions of mixtures containing 0.1, 0.5, 1 and 1.5 wt% meteorite component, with results portrayed in Fig. 11. Our results show that addition of ~0.5 wt% of a meteorite component is sufficient to raise mantle abundances to their current level and erase the original signature of metal-silicate equilibrium (we note that the EH chondrite additive works best in this model, as ~0.3 wt% of this component simultaneously reproduces the primitive mantle concentrations of all three elements). Is this amount of exogenous additive consistent with mantle abundances of the highly siderophile elements? As mentioned in Section 1, results of metal-silicate partitioning experiments for some highly siderophile elements indicate that core formation will result in their quantitative removal from the silicate Earth (e.g., Pt: Holzheid et al., 2000; Fortenfant et al., 2003; Ertel et al., 2006; Os: Fortenfant et al., 2006; Yokoyama et al., 2009), whereas recent results for Pd and Au suggest less extreme partitioning, resulting in silicate concentrations similar to primitive mantle (Danielson et al., 2005; Richter et al., 2008). For the case of quantitative removal of the HSEs (i.e., estimate $D^{\text{metal/silicate}}$ of $>10^5$), taking Os as an example, the mean Os content of H-type chondrite is 820 ppb (Wasson and Kallemeyn, 1988; other ordinary chondrites are similar), so addition of 0.5 wt% of this component to a mantle stripped of Os would result in a concentration of 4.1 ppb, similar to the value of $3.9 (\pm 0.5)$ ppb estimated for primitive mantle (Becker et al., 2006). In the case of less extreme partitioning, recent results for Pd yield a value of $D^{\text{metal/silicate}}$ for core-forming conditions of 300 (+400/–100) (Richter et al., 2008). Taking the uncertainty in this value into account, calculated mantle abundances resulting from metal-silicate equilibrium range from 2.5 to 8.6 ppb. Addition of 0.5 wt% of H-type chondrite with 870 ppb Pd (mean value from Wasson and Kallemeyn, 1988) to this mantle would yield abundances of 6.8–12.9 ppb, which are similar to the estimated primitive mantle value of $7.1 (\pm 1.3)$ ppb (Becker et al., 2006). Thus, it seems that the small amount of exogenous additive required to raise abundances of Te, Se and S to primitive mantle levels is also sufficient to account for mantle abundances of the highly siderophile elements.

6. CONCLUSIONS

Abundances of Te, Se, and S in upper mantle xenoliths, their included sulfides, and primitive MORB magmas sug-

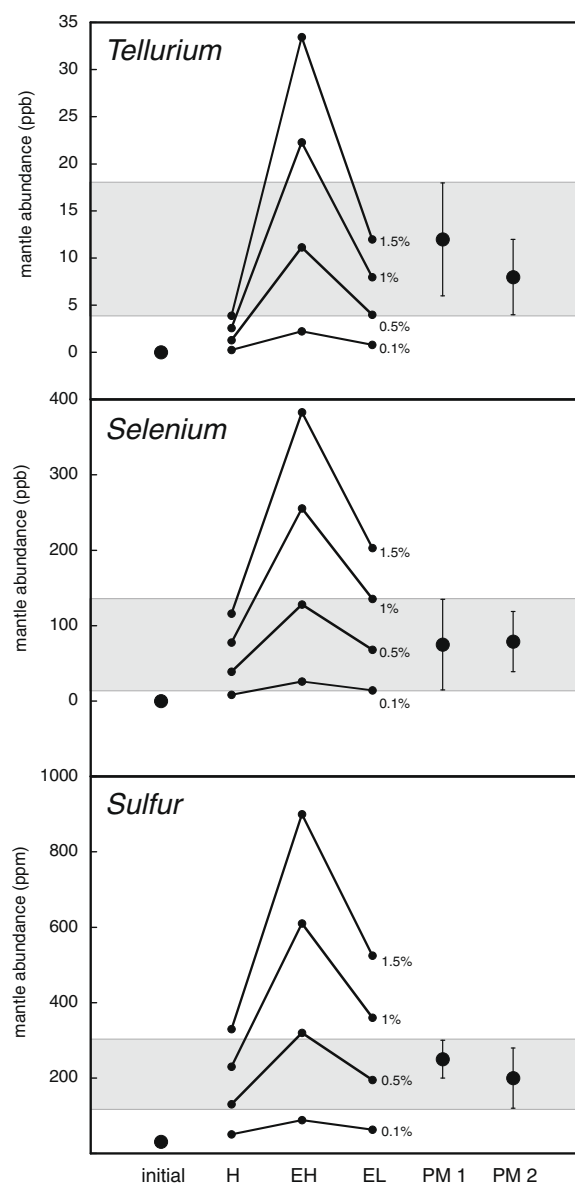


Fig. 11. Comparison between calculated concentrations of Te, Se, and S in the mantle after core formation, 'refertilization' by various types of ordinary chondrite, and values estimated for the primitive mantle (PM1 = McDonough and Sun, 1995; PM2 = Palme and O'Neill, 2003; Table 1). The shaded area represents the estimated error in the PM concentration.

gest these elements are present in the primitive mantle at near-chondritic relative proportions, although depleted 100-fold from a volatile-corrected CI-chondrite-Mg-normalized composition. Measurements of liquid metal–liquid silicate partitioning over a range of pressure, temperature, and oxygen fugacity were done to determine the extent to which these abundances were established by metal-silicate equilibrium during a magma ocean stage early in Earth's history. Under most conditions studied, $D_{\text{Te}} > D_{\text{Se,S}}$, and both Te and Se become more siderophile with the addition of S to the system. Theory predicts that metal-silicate

partitioning of these elements will be *independent* of fO_2 , but sensitive to changes in the both activity of FeO, and the equilibrium constant governing the solution of Te, Se, and S, in the silicate phase. We have found that the metal-silicate partition coefficients for Te, Se, and S increase with increasing fO_2 , which, in the case of sulfur, can be adequately modeled as arising from variation in a_{FeO} , as sample redox is governed by the Fe–FeO equilibrium. Te, Se, and S all become more siderophile with increasing pressure and less siderophile with increasing temperature.

The partitioning behaviour measured in experiments is generally consistent with the relative Te–Se–S fractionation seen in natural systems, which have evolved by sulfur-rich metallic liquid–silicate liquid equilibrium. For example, the Te/Se in mantle sulfide is higher than in conjugate silicate magmas, consistent with greater compatibility of Te relative to Se in residual S-bearing metallic melt. The fractionated Se/S seen in primitive melts relative to their source is consistent with the partitioning behaviour of Se and S in metallic melts with high S content (e.g. experiment BGI-A).

The combined pressure and temperature dependence to partitioning is estimated by multivariate regression to predict the metal-silicate partitioning behaviour of Te, Se, and S along the peridotite liquidus in a deepening magma ocean. Results of this model predict that the absolute concentrations of Te and Se will be substantially lower than the estimated primitive mantle compositions, and ratios of Te/Se and Te/S are distinctly non-chondritic. This result leads us to favour a model in which the mantle remained open to inputs of Te, Se and S-bearing material during late accretion, consistent with results for the highly siderophile elements. The addition of small amounts of a ‘late veneer’ comprised of H-, EH- or EL-type chondrite could have provided the necessary material to refertilize the mantle abundances of Te, Se, S.

ACKNOWLEDGMENTS

Werner Ertel, Hugh O'Neill, and Dave Walker provided helpful reviews of an earlier version of this manuscript. Nancy Chabot and two anonymous reviewers are thanked for their thoughtful reviews of the current manuscript. This work was supported by a NSERC doctoral scholarship and post-doctoral funding from the Bayerisches Geoinstitut to LRW, and Discovery and Equipment grants to JMB at the University of Toronto and to RAS at the University of Western Ontario. Penny King is thanked for lending piston-cylinder equipment, and we acknowledge the technical assistance of Colin Bray, Mike Gorton, Oleg Bogdanovski, Detlef Krauß, and Andreas Audétat.

APPENDIX A. SUPPLEMENTARY DATA

Supplementary data associated with this article can be found, in the online version, at [doi:10.1016/j.gca.2009.04.028](https://doi.org/10.1016/j.gca.2009.04.028).

REFERENCES

Allègre C. J., Poirier J.-P., Humler E. and Hofmann A. W. (1995) The chemical composition of the Earth. *Earth Planet. Sci. Lett.* **134**, 515–526.

- Anders E. (1977) Chemical compositions of the Moon, Earth, and eucrite parent body. *Philos. Trans. Roy. Soc. Lond.* **A295**, 23–40.
- Asahara Y., Frost D. J. and Rubie D. C. (2007) Partitioning of FeO between magnesiowüstite and liquid iron at high pressures and temperatures: implications for the composition of the Earth's outer core. *Earth Planet. Sci. Lett.* **257**, 435–449.
- Becker H., Horan M. F., Walker R. J., Gao S., Lorand J.-P. and Rudnick R. L. (2006) Highly siderophile element composition of the Earth's primitive upper mantle: constraints from new data on peridotite massifs and xenoliths. *Geochim. Cosmochim. Acta* **70**, 4528–4550.
- Benz W. and Cameron, A. G. W. (1990) Terrestrial effects of the giant impact. In: *Origin of the Earth and Moon*. (eds. H. E. Newsom and J. H. Jones). pp. 61–67.
- Boettcher A. L., Burnham C. W., Windom K. E. and Bohlen S. R. (1982) Liquids, glasses, and the melting of silicates to high pressures. *J. Geol.* **90**(2), 127–138.
- Brandon A. D., Walker R. J. and Puchtel I. S. (2006) Platinum–osmium isotope evolution of the Earth's mantle: constraints from chondrites and Os-rich alloys. *Geochim. Cosmochim. Acta* **70**, 2093–2103.
- Brenan J. M., McDonough W. F. and Dalpé C. (2003) Experimental constraints on the partitioning of rhenium and some platinum-group elements between olivine and silicate melt. *Earth Planet. Sci. Lett.* **212**, 135–150.
- Brenan J. M. and McDonough W. F. (2006) Sulfide-silicate Partitioning of Mo, Sb, Pb, Se, and Te: Initial Results. GACMAC Montreal.
- Bulanova G. P., Griffin W. L., Ryan C. G., Shestakova O. Ye. and Barnes S.-J. (1996) Trace elements in sulfide inclusions from Yakutian diamonds. *Contrib. Mineral. Petrol.* **124**, 111–125.
- Chabot N. L., Draper D. S. and Agee C. B. (2005) Conditions of core formation in the Earth: constraints from nickel and cobalt partitioning. *Geochim. Cosmochim. Acta* **69**, 2141–2151.
- Choi N. and Cho W. D. (1997) Distribution behavior of cobalt, selenium, and tellurium between nickel–copper–iron matte and silica-saturated iron silicate slag. *Metall. Mater. Trans. B* **28**, 429–438.
- Cottrell E. and Walker D. (2006) Constraints on core formation from Pt partitioning in mafic silicate liquids at high temperatures. *Geochim. Cosmochim. Acta* **70**, 1565–1580.
- Danielson L., Sharp T., Hervig R. L. (2005) Implications for core formation of the Earth from high pressure-temperature Au partitioning experiments. In *36th Lunar and Planetary Science Conference*. No. 1955 (abstr.).
- Eggins S. M., Kinsley L. P. J. and Shelley J. M. G. (1998) Deposition and element fractionation processes during atmospheric pressure laser sampling for analysis by ICPMS. *Appl. Surf. Sci.* **129**, 278–286.
- Ertel W., Walter M. J., Drake M. J. and Sylvester P. J. (2006) Experimental study of platinum solubility in silicate melt to 14 GPa and 2273 K: implications for accretion and core formation in Earth. *Geochim. Cosmochim. Acta* **70**, 2591–2602.
- Fincham C. J. B. and Richardson F. D. (1954) The behaviour of sulphur in silicate and aluminate melts. *Proc. Roy. Soc. A* **223**, 4062.
- Fortenfant S. S., Gunther D., Dingwell D. B. and Rubie D. C. (2003) Temperature dependence of Pt and Rh solubilities in a haplobasaltic melt. *Geochim. Cosmochim. Acta* **67**(1), 123–131.
- Fortenfant S. S., Dingwell D. B., Ertel-Ingrisch W., Capmas F., Birk J. L. and Dalpé C. (2006) Oxygen fugacity dependence of Os solubility in haplobasaltic melts. *Geochim. Cosmochim. Acta* **70**, 742–756.
- Ganapathy R., and Anders E. (1974) Bulk compositions of the Moon and Earth, estimated from meteorites. In *5th Lunar Conference*. pp. 1181–1206.

- Garuti G., Gorgoni C. and Sighinolfi G. P. (1984) Sulfide mineralogy and chalcophile and siderophile element abundances in the Ivrea-Verbano mantle peridotites (Western Italian Alps). *Earth Planet. Sci. Lett.* **70**, 69–87.
- Günther D. and Heinrich C. A. (1999) Enhanced sensitivity in laser ablation-ICP mass spectrometry using helium–argon mixtures as aerosol carrier. *J. Anal. Atom. Spectrom.* **14**, 1363–1368.
- Halliday A. N. (2004) Mixing, volatile loss and compositional change during impact-driven accretion of the Earth. *Nature* **427**, 505–509.
- Hamlyn P. R., Keays R. R., Cameron W. E., Crawford A. J. and Waldron H. M. (1985) Precious metals in magnesian low-Ti lavas: implications for melaogenesis and sulfur saturation in primary magmas. *Geochim. Cosmochim. Acta* **49**, 1797–1811.
- Hattori K. H., Arai S. and Clarke D. B. (2002) Selenium, tellurium, arsenic, and antimony contents of primary mantle sulfides. *Can. Mineral.* **40**, 637–650.
- Haughton D. R., Roeder P. L. and Skinner B. J. (1974) Solubility of sulfur in mafic magmas. *Econ. Geol.* **69**, 451–467.
- Hertogen J., Janssens M. J. and Palme H. (1980) Trace elements in ocean ridge basalt glasses: implications for fractionations during mantle evolution and petrogenesis. *Geochim. Cosmochim. Acta* **44**, 2125–2143.
- Holzheid A., Sylvester P., O'Neill H. St. C., Rubie D. C. and Palme H. (2000) Evidence for a late chondritic veneer in the Earth's mantle from high-pressure partitioning of palladium and platinum. *Nature* **406**, 396–399.
- Jarosewich E. (1990) Chemical analyses of meteorites: a compilation of stony and iron meteorite analyses. *Meteoritics* **25**, 323–337.
- Kavner A. and Jeanloz R. (1998) High pressure melting curve of platinum. *J. Appl. Phys.* **83**, 7553–7559.
- Kegler Ph., Holzheid A., Frost D. J., Rubie D. C., Dohmen R. and Palme H. (2008) New Ni and Co metal-silicate partitioning data and their relevance for an early terrestrial magma ocean. *Earth Planet. Sci. Lett.* **268**, 28–40.
- Kilburn M. R. and Wood B. J. (1997) Metal-silicate partitioning and the incompatibility of S and Si during core formation. *Earth Planet. Sci. Lett.* **152**, 139–148.
- Kleine T., Palme H., Mezger M. and Halliday A. N. (2005) Hf-W chronometry of lunar metals and the age and early differentiation of the Moon. *Science* **310**, 1671–1674.
- Kress V. (2007) Thermochemistry of sulfide liquids III: Ni-bearing liquids at 1 bar. *Contrib. Mineral. Petrol.* **154**, 191–204.
- Li J. (2000) Element Partitioning Constraints on Core–mantle Differentiation. Ph.D. Thesis, Harvard University.
- Li J. and Agee C. B. (1996) Geochemistry of mantle-core differentiation at high pressure. *Nature* **381**, 686–689.
- Lipovskii A. A., Melekhin V. G., Petrikov V. D. and Tatarintsev B. V. (2008) Influence of reduction–oxidation synthesis conditions on the nature of color centers in silicate glass doped with selenium. *Glass Phys. Chem.* **34**(2), 155–159.
- Lodders K. (2003) Solar system abundances and condensation temperatures of the elements. *Astrophys. J.* **591**(2), 1220–1247.
- Longerich H. P., Jackson S. E. and Günther D. (1996) Laser ablation inductively coupled plasma mass spectrometric transient signal data acquisition and analyte concentration calculation. *J. Anal. Atomic Spectrom.* **11**, 899–904.
- Lorand J. P. (1990) Are spinel lherzolite xenoliths representative of the abundance of sulfur in the mantle? *Geochim. Cosmochim. Acta* **54**, 1487–1492.
- Lorand J. P., Alard O., Luguët A. and Keays R. R. (2003) Sulfur and selenium systematics of the subcontinental lithospheric mantle: inferences from the Massif Central xenolith suite (France). *Geochim. Cosmochim. Acta* **67**(21), 4137–4151.
- McDonough W. M. and Sun S.-S. (1995) The composition of the Earth. *Chem. Geol.* **120**(3–4), 223–253.
- Mavrogenes J. A. and O'Neill H. St. C. (1999) The relative effects of pressure, temperature and oxygen fugacity on the solubility of sulfide in mafic magmas. *Geochim. Cosmochim. Acta* **63**, 1173–1180.
- Meisel T., Walker R. J., Irving A. J. and Lorand J.-P. (2001) Osmium isotopic compositions of mantle xenoliths: a global perspective. *Geochim. Cosmochim. Acta* **65**, 1311–1323.
- Metrich N., Berry A., O'Neill H. St. C. and Susini J. (2005) A XANES study of sulfur speciation in synthetic glasses and melt inclusions. *Geochim. Cosmochim. Acta* **69**(10), A51.
- Morgan J. W. (1985) Osmium isotope constraints on Earth's late accretionary history. *Nature* **317**, 703–705.
- Morgan J. W. (1986) Ultramafic xenoliths: clues to Earth's late accretionary history. *J. Geophys. Res.* **91**(B12), 12375–12387.
- O'Neill H. St. C. and Eggins S. M. (2002) The effect of melt composition on trace element partitioning: an experimental investigation of the activity coefficients of FeO, NiO, CoO, MoO₂ and MoO₃ in silicate melts. *Chem. Geol.* **186**, 151–181.
- Ohtani E., Yurimoto H. and Seto S. (1997) Element partitioning between metallic liquid, silicate liquid, and lower mantle minerals: implications for core formation of the Earth. *Phys. Earth Planet. Interiors* **100**, 97–114.
- Palme H. and O'Neill H. St. C. (2003) Cosmochemical estimates of mantle composition. *Treatise Geochem.* **2**, 1–38.
- Peach C. L., Mathez E. A. and Keays R. R. (1990) Sulfide melt-silicate melt distribution coefficients for noble metals and other chalcophile elements as deduced from MORB: implications for partial melting. *Geochim. Cosmochim. Acta* **54**, 3379–3389.
- Righter K. and Drake M. J. (1997) Metal-silicate equilibrium in a homogeneously accreting earth: new results for Re. *Earth Planet. Sci. Lett.* **146**, 541–553.
- Righter K., Humayun M. and Danielson L. (2008) Partitioning of palladium at high pressures and temperatures during core formation. *Nature*. doi:10.1038/ngeo180.
- Righter K., Drake M. J. and Yaxley G. (1997) Prediction of siderophile element metal/silicate partition coefficients to 20 GPa and 2800 °C: the effects of pressure, temperature, oxygen fugacity, and silicate and metallic melt compositions. *Phys. Earth Planet. Interiors* **100**, 115–142.
- Sasaki S. and Nakazawa K. (1986) Metal-silicate fractionation in the growing Earth: energy source for the terrestrial magma ocean. *J. Geophys. Res.* **91**, B9231–B9238.
- Toplis M. J. (2005) The thermodynamics of iron and magnesium partitioning between olivine and liquid: criteria for assessing and predicting equilibrium in natural and experimental systems. *Contrib. Mineral. Petrol.* **149**, 22–39.
- Tonks W. B. and Melosh H. J. (1993) Magma ocean formation due to giant impacts. *J. Geophys. Res. Planets* **98**(E3), 5319–5333.
- van Westrenan W., Van Orman J. A., Watson H., Fei Y. and Watson E. B. (2003) Assessment of temperature gradients in multi-anvil assemblies using spinel layer growth kinetics. *Geochim. Geophys. Geosyst.* **4**(4). doi:10.1029/2002GC000474.
- Wade J. and Wood B. J. (2005) Core formation and the oxidation state of the Earth. *Earth Planet. Sci. Lett.* **236**, 78–95.
- Watson E. B., Wark D. A., Price J. D. and Van Orman J. A. (2002) Mapping the thermal structure of solid-media pressure assemblies. *Contrib. Mineral. Petrol.* **142**, 640–652.
- Wasson J. T. and Kallemeyn G. W. (1988) Compositions of chondrites. *Philos. Trans. Roy. Soc. Lond. A Math. Phys. Sci.* **325**(1587), 535–544.
- Wetherill G. W. (1994) Provenance of the terrestrial planets. *Geochim. Cosmochim. Acta* **58**, 4513–4520.

- Wolf R., Richter G. R., Woodrow A. B. and Anders E. (1980) Chemical fractionations in meteorites: XI. C2 chondrites. *Geochim. Cosmochim. Acta* **44**, 711–717.
- Wood B. J., Walter M. J. and Wade J. (2006) Accretion of the Earth and segregation of its core. *Nature* **441**, 825–833.
- Yokoyama T., Walker D. and Walker R. J. (2009) Low osmium solubility in silicate at high pressures and temperatures. *Earth Planet. Sci. Lett.* **279**, 165–173.

Associate editor: Richard J. Walker